ACS APPLIED MATERIALS & INTERFACES

www.acsami.org

Research Article

Effect of Tyrosine-Containing Self-Assembling β-Sheet Peptides on Macrophage Polarization and Inflammatory Response

Jacek K. Wychowaniec,* Ezgi Irem Bektas, Marcia Muerner, Jiranuwat Sapudom, Martin Šrejber, Marielle Airoldi, Roland Schmidt, Andrea J. Vernengo, Charlotte J. C. Edwards-Gayle, Paul Sean Tipay, Michal Otyepka, Jeremy Teo, David Eglin, and Matteo D'Este

Cite This: ACS Appl. Mater. Interfaces 2025, 17, 27740−27758

Read Online

ACCESS | Metrics & More | Article Recommendations | Supporting Information

ABSTRACT: Self-assembling peptides (SAPs) are fully defined nanobiomaterials offering unprecedented opportunities to control nanostructure and chemical attributes to investigate and manipulate cellular signals. To investigate the influence of chemical and morphological characteristics on inflammatory signaling in native immunity, we designed five β-sheet SAPs: EFEFKFEFK (**EF8**), YEFEFKFEFK (**YEF8**), EFEFKFEFK**Y** (**EF8Y**), YEFEFKFEFK**Y** (**YEF8Y**), and EYEFKFEFK (**EYF8**) (F: phenylalanine; E: glutamic acid; K: lysine, **Y**: tyrosine). The position of tyrosine in the peptide sequence dictated the self-assembly into nanostructures, with all SAPs self-assembling into thin constituent nanofibers with $d \approx 3.8 \pm 0.4$ nm, and sequences **YEF8** and **EF8** showing a propensity for associative bundling. These distinct SAPs induced contrasting inflammatory responses of monocytic model THP-1 cells-derived macrophages (MΦs). Presence of soluble **EF8** nanofibers (at 2 mM) induced an anti-inflammatory response and polarization toward an M2 state, whereas **YEF8** (at 2 mM) displayed a tendency for inducing a pro-inflammatory response and polarization toward an M1 state. **EF8Y**, **YEF8Y**, and **EYF8** SAPs did not induce an inflammatory response in our models. These results were validated using peripheral blood mononuclear cells (PBMCs)-derived MΦs from human donors, confirming the critical role of **EF8** and **YEF8** SAPs as possible orchestrators of the repair of tissues or inducers of pro-inflammatory state, respectively. The same MΦs polarization responses from THP-1-derived MΦs cultured on 20 mM hydrogels were obtained. These findings will facilitate the utilization of this family of SAPs as immunomodulatory nanobiomaterials potentially changing the course of inflammation during the progression of various diseases.

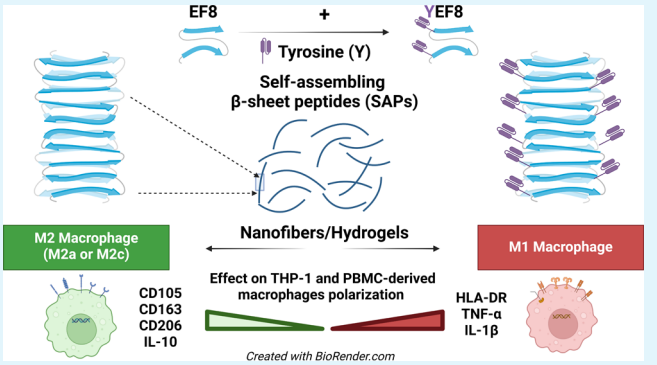

KEYWORDS: *tyrosine-modified self-assembling peptides, nanostructured peptides, macrophage polarization, inflammation, immunomodulation*

1. INTRODUCTION

Multifunctional biomaterials which exhibit well-defined physicochemical properties and encode spatiotemporally controlled biological signals are emerging as advanced systems for cell culture and organoids growth. Producing and manipulating complex immunological signals is critical for achieving effective tissue regeneration,[1] as both innate and adaptive immune systems play essential roles in inflammation-mediated healing.[2,3] While inflammation triggers tissue repair after injury, chronic inflammation is detrimental, and the balance between these outcomes is context-dependent.[4] These effects are linked to immune cell phenotypes at the injury site and the chosen treatment method, involving dendritic cells, monocytes, neutrophils, macrophages (MΦs), T-cells, and B-cells, alongside cytokines, chemokines, and growth factors. Together, these components form a complex system that orchestrates healing.[5]

MΦs are central to wound healing,[6] producing cytokines and chemokines that drive tissue toward homeostasis.[7] They exist on a polarization spectrum, from a pro-inflammatory M1 state (classically activated) to anti-inflammatory M2-like (alternatively activated) states.[1,8] M1 MΦs respond to pathogens, interferon-γ (IFN-γ), and lipopolysaccharides (LPS), producing high levels of pro-inflammatory cytokines (e.g., IL-1β, IL-6, and TNF-α), promoting inflammation and preparing the wound to repair. In contrast, M2 MΦs (covering M2a, M2b, M2c, and M2d) respond to signals such as IL-4, IL-

Received: November 14, 2024
Revised: February 14, 2025
Accepted: April 1, 2025
Published: April 16, 2025

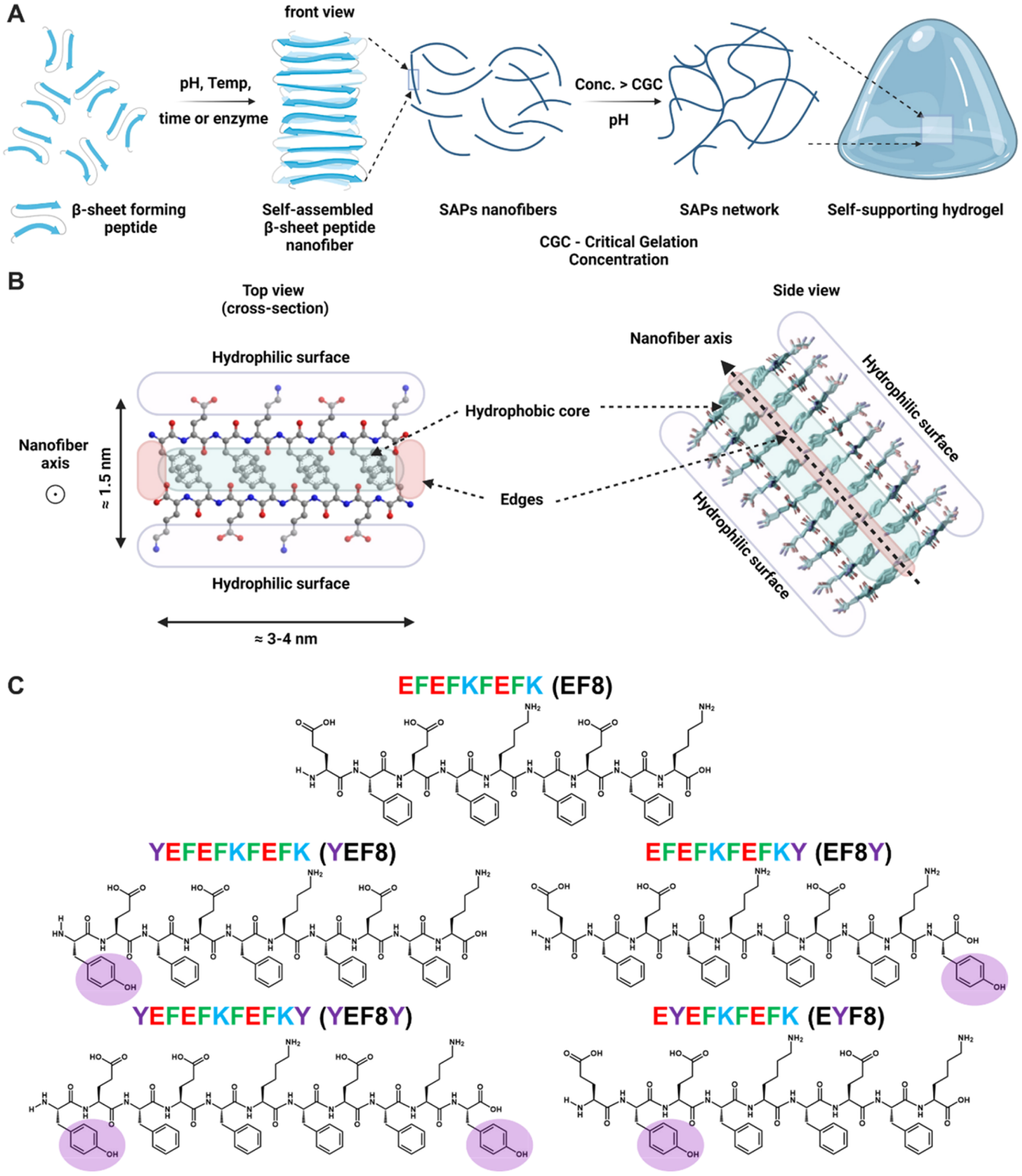

Figure 1. (A) Schematic representation of the self-assembly and gelation pathway of *β*-sheet forming peptides. Created with BioRender.com. (B) A scheme of the formed nanofibers depicting top and side views. The peptide illustrated here is an original sequence FEFKFEFK (**F8**) (F: phenylalanine, E: glutamic acid, K: lysine), used for the inclusion of tyrosine. The three shadings depict the relevant areas of nanofibers: hydrophilic surface, hydrophobic core, and edges. Partly created with BioRender.com. (C) Chemical structures of peptides used in this study. Sequence **EF8** is a derivation of the original **F8** by the inclusion of glutamic acid, whereas all further sequences are tyrosine-modified versions of **EF8**. Tyrosine is highlighted in purple.

13, IL-10, and TGF*β*, aiding tissue remodeling and repair depending on the subtype.[9,10] The dynamic ratio of MΦ phenotypes during healing is critical, with M1 dominating early inflammation and M2 driving resolution and repair over time.

https://doi.org/10.1021/acsami.4c19900
ACS Appl. Mater. Interfaces 2025, 17, 27740−27758

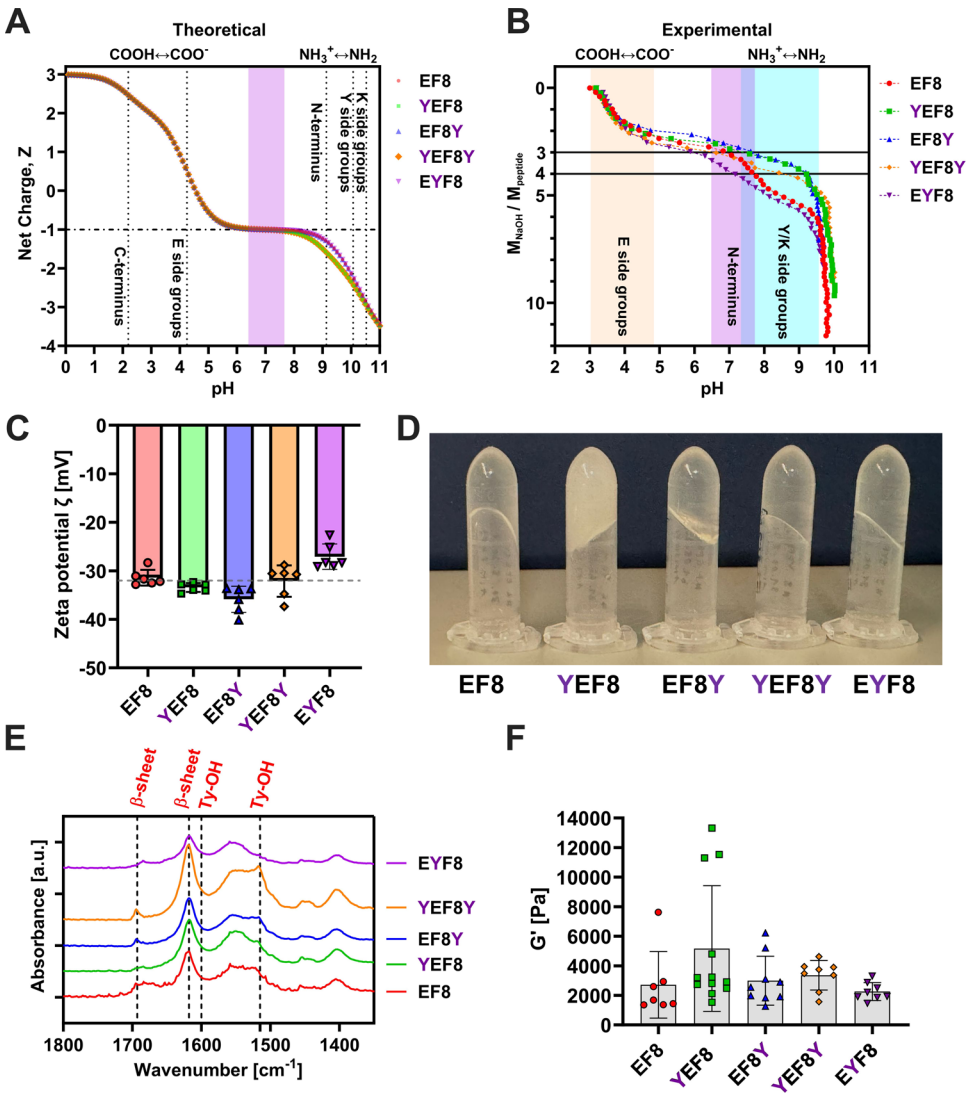

Figure 2. (A) Theoretical charge carried by each peptide as a function of pH. Vertical dotted lines indicate the theoretical pK_a of the different ionic groups present on the peptides. The shaded region depicts physiological conditions. The horizontal dotted line depicts a charge state at physiological conditions of $Z = -1$ e$^-$. Note that curves for **EF8**, **EF8Y**, and **EYF8**, as well as **YEF8** and **YEF8Y**, closely overlap altogether, respectively. (B) The molar ratio of added NaOH to peptide as a function of pH. Shadowed regions indicate the protonation/deprotonation transition regions of the different ionic groups (E: Glutamic acid, K: Lysine, Y: Tyrosine). The horizontal lines depict a region of 3−4 equiv of deprotonation of moles of peptide. Theoretically, 3 mol equiv of NaOH is required to deprotonate all glutamic acids present in each peptide. (C) ζ-Potential values obtained for all SAPs at pH 7.1 ± 0.2. The dashed gray line depicts −32 mV. (D) Photograph of SAP hydrogels prepared at 20 mM and physiological pH. (E) ATR-FTIR spectra obtained for all hydrogels prepared at a concentration of 20 mM. Vertical dashed lines indicate the position of the two bands characteristic of adoption by peptides of β-sheet conformations as well as tyrosine-specific peaks. (F) Storage modulus (G') for different designed peptide hydrogels at 20 mM concentration taken at ∼0.162% strain and 1 Hz frequency from multiple amplitude sweeps and at 0.2% strain and 1 Hz from frequency sweeps. In total, 5−6 repeats of independently prepared hydrogels are shown. Amplitude sweeps are provided in the Supporting Information (Figure S3).

Biomaterials provide biochemical and physical cues to modulate MΦ phenotypes.[11] Recent studies highlight biomaterials' immunomodulatory properties in mitigating damaging inflammatory responses and enhancing tissue repair.[12,13] This process was shown to be important in inducing enhanced bone formation by either promotion of vascular invasion and instructed earlier inflammation[12] or prolonged shift toward M2 MΦ phenotype.[13] Further, nanofibers (>100 nm), often produced via electrospinning from materials such as polycaprolactone (PCL), can influence MΦ phenotypes, primarily promoting M2 polarization.[14,15] However, few studies have explored the effects of smaller (<100 nm) self-assembled nanofibers on MΦ behavior,[16] warranting further investigation into their chemical composition and structural impact on immune modulation.

Molecular self-assembly is a process where molecules spontaneously organize into higher nanostructures via noncovalent interactions.[17] Among these, self-assembling peptides (SAPs) are particularly notable due to their high fidelity, purity, and cost-effective synthesis, avoiding batch-to-batch variations.[18] SAPs, composed of natural amino acids, can be designed to promote or inhibit specific cellular processes.[19] Minimalistic approaches allow for identifying short peptide sequences prone to forming targeted nanostructures.[20] Many peptides self-assemble into fibers and form hydrogels above a critical gelation concentration (CGC).[21] By tailoring their

https://doi.org/10.1021/acsami.4c19900
ACS Appl. Mater. Interfaces 2025, 17, 27740−27758

primary sequences, functional materials with defined nanostructures and responsiveness can be developed.[21,22]

β-sheet SAPs are an attractive class of biomaterials, particularly for hydrogels and emulgels/emulsions.[23,24] These highly hydrated materials can mimic extracellular matrix (ECM),[25] exhibit biocompatibility, and are tunable in their physicochemical and biological properties. They also hold potential for additive manufacturing[26] and as platforms for growing organoids and cellular spheroids.[27] Zhang's group pioneered one of the most successful SAP designs: $(\mathbf{ABACABAC})_n$, which alternates hydrophobic (**A**) and hydrophilic (**B**/**C**) amino acids.[28] These self-assemble into nanofibers (2−10 nm diameter) and form self-supporting hydrogels above CGC (Figure 1A). Their nanofiber structure features hydrophilic outer surface, hydrophobic core, and distinct edges that mediate interactions with other nanofibers and external molecules, such as drugs or cells (Figure 1B).[29,30]

Chemical modifications to SAPs, including edge substitutions, influence nanostructure formation and hydrogel properties.[24,26,29,30] For instance, Collier's group demonstrated that SAPs can act as adaptive immunomodulators, adjuvants, and vaccine platforms.[31−33] They also demonstrated that a peptide FKFEFKFE (KFE8) does not trigger adaptive immunity.[34] Negatively charged SAP surfaces suppress T-cell and antibody responses, while positively charged surfaces enhance peptide uptake by antigen-presenting cells.[35] Similarly, Kumar et al. reported nonimmunogenic β-sheet SAPs that modulated THP-1-derived MΦs only when codelivering Monocyte Chemoattractant Protein-1 (MCP-1) and IL-4,[16] highlighting their potential as delivery platforms.

Given that β-sheet SAP nanofibers are generally nonimmunogenic, we sought to explore their ability to modulate native immunity through chemical or nanostructural modifications. Tyrosine, a versatile amino acid,[36] enables functional material assembly and cross-linking, enhancing viscoelastic properties and material stability.[37] Previously, we demonstrated that tyramine-modified hyaluronic acid exhibited minimal pro-inflammatory responses, with molecular weight influencing macrophage polarization.[38] Unlike hyaluronic acid or collagen-based therapies,[39,40] SAP chemical modifications offer a broader design space to modulate inflammation without compromising physicochemical properties. Hence, in this study, we introduce tyrosine-modified β-sheet SAPs: EFEFKFEFK (**EF8**), **Y**EFEFKFEFK (**YEF8**), EFEFKFEFK**Y** (**EF8Y**), **Y**EFEFKFEFK**Y** (**YEF8Y**), and E**Y**EFKFEFK (**EYF8**) (F: phenylalanine; E: glutamic acid; K: lysine, **Y**: tyrosine) (Figure 1C). **EF8**, a derivative of the well-characterized FEFKFEFK (**F8**) peptide, was used as a control, forming thin, negatively charged nanofibers ($Z \approx -1$ at physiological pH).[41] Tyrosine was incorporated at the N-terminus (**YEF8**), C-terminus (**EF8Y**), both N- and C-termini (**YEF8Y**), or within the core (**EYF8**). These modifications created a new family of tyrosine-containing SAPs.

We evaluated their self-assembly and gelation using titrations, electrophoretic light scattering (ELS), rheology, Fourier transform infrared spectroscopy (FTIR), thioflavin T (ThT) binding assay, transmission electron microscopy (TEM), scanning electron microscopy (SEM), and small-angle X-ray scattering (SAXS). Functional assessment of these SAPs focused on their ability to modulate MΦ polarization. We screened their immunomodulatory potential using monocytic THP-1 cells-derived MΦs and validated findings with peripheral blood mononuclear cells (PBMCs)-derived MΦs for clinical relevance. M1/M2-like polarization was analyzed via immunocytochemistry, flow cytometry, gene expression, and ELISAs. Cytotoxicity was tested on THP-1-derived MΦs, mouse fibroblasts, and primary human fibroblasts. Finally, we correlated distinct physicochemical SAP features with inflammatory profiles to establish design principles for immunomodulatory nanobiomaterials. These insights aim to advance tissue engineering and biofabrication applications by integrating biocompatibility and stable MΦ polarization into SAP design.

2. RESULTS AND DISCUSSION

2.1. Self-assembly, Charge Profiling, and Gelation Properties. The charge of SAPs has been shown to affect the immunogenicity and interactions with immune cells.[35] To evaluate this, we assessed the charge behavior of our selected SAPs at physiological pH. All peptides self-assembled into hydrogels above CGC of ≈2.5 mM (Figure S1). All samples below CGC were clear solutions. Hydrophilic amino acids in the peptides contain ionic groups (Figure 1C) that can deprotonate at specific theoretical pK_a values: carboxylic acid (COOH) at the C-terminus (p$K_a \approx 2.18$) and on the glutamic acid side chains (p$K_a \approx 4.25$) and amine (NH_2) at the N-terminus (p$K_a \approx 9.13$ and ≈ 8.95 on F and K sides, respectively) and on the lysine side chains (p$K_a \approx 10.53$),[42] as well as (OH) side group on tyrosine (p$K_a \approx 10.07$), which can also form hydrogen bonds.[42,43] Past studies have shown that self-assembly can alter apparent pK_a values due to the changes in the chemical environment,[30] affecting electrostatic interactions and gelation properties of this family of β-sheet forming peptides.[30,44]

Figure 2A shows the theoretical charge carried by all of the peptides across pH, with each peptide carrying a charge of $Z \approx -1$ at physiological pH. To verify the effects of self-assembly, we titrated each peptide in a clear solution state at a concentration of 1 mM (Figure 2B) and measured their ζ-potential at 0.2 mM (Figure 2C). This range of concentrations is typically larger than the minimum fibrillization (i.e., critical aggregation) concentration of this class of SAPs, noted to be in the range of 50−100 μM.[45] All peptides were purchased as HCl salts, initially presenting an acidic pH (3.1 ± 0.2), above the theoretical pK_a of the C-terminal COOH groups, which are hence deprotonated.[30] Upon NaOH addition, carboxylic acids on glutamic acid deprotonated between pH 3.0 and 4.8. Owing to electrostatic factors, the final glutamic acid, close to lysine residues, required more base, with full deprotonation occurring at slightly varied pH values across SAPs (Figure 2B). Previously, it has been shown that the transition from cloudy to clear hydrogels in these SAPs correlates with the increase in interpeptide electrostatic repulsion, when the modulus of charge $|Z| > 1$.[30,46] All SAPs also form self-supporting clear hydrogels (above similar CGC ∼ 2.5 mM) except for **YEF8**, which retained cloudiness at physiological pH and at 20 mM concentration (Figure 2D). Considering that fact and the detailed aspects of the subsequent deprotonation of the NH_3^+ side chains occurring later, titrations reveal that all SAPs carry a charge in the range $-2 \le Z \le -1$ at physiological pH (7.2 ± 0.2). ζ-Potential measurements confirmed that **EF8**, **YEF8**, **EF8Y**, and **YEF8Y** SAPs all carry a charge close to −32 mV, whereas **EYF8** carries a value of −27.1 ± 2.6 mV (Figure 2C). Given the similarly in charge status, observed immunological effects among SAPs are unlikely to be due to charge

https://doi.org/10.1021/acsami.4c19900
ACS Appl. Mater. Interfaces 2025, 17, 27740−27758

differences. Consequently, all SAPs solutions and hydrogels were prepared within this pH range.

The β-sheet conformation was confirmed using ATR-FTIR (Figure 2E), thioflavin-T (ThT) binding assay (Figure S2A,B), and CD spectroscopy (Figure S2C,D). All peptides were characterized by strong transmittance bands at 1618 cm^{-1} and bands in the region of 1684−1693 cm^{-1} (Figure 2E), characteristic of the adoption by the peptides of β-sheet conformations.[47] The β-sheet conformation was corroborated by the enhancement of ThT fluorescence intensity which peaked at λ = 490 nm, both for SAPs at 2 mM (below CGC, Figure S2A) and for SAP hydrogels prepared at 20 mM (Figure S2B). Finally, we utilized CD spectroscopy, where we observed a strong negative band centered in the range of 204−218 nm, and a strong positive peak centered at 192 nm (Figure S2C). We attempted to deconvolute these spectra (Figure S2D), where around 43% secondary structure was obtained in the form of β-sheet strand/turn conformations for all SAPs, except **EF8**, for which only 6% was obtained (Figure S2D). Here, we want to emphasize that the accuracy of this deconvolution method is strongly obscured by the propensity of SAPs to align,[48] such as in the case of **EF8** SAPs noticed during later evaluations. This method also relies on the limited availability of secondary structure referencing, stemming only from pure protein databanks.[49,50] Hence, we do not solely rely on this methodology and utilize their combinations, including molecular dynamics (MD) described later.

Viscoelastic features of soft materials have been shown to be a key cell-instructing factor,[51] and we have also previously shown the influence of variable stiffness of peptide hydrogels in the development of organoids.[27] Therefore, for all bulk hydrogels, prepared at 20 mM concentration, we run amplitude (Figure S3) and frequency (Figure S4) sweeps. We found that storage modulus (G') was typically an order of magnitude larger than loss modulus (G'') in the linear viscoelastic region (LVR, Figure S3) and in the linear frequency region (Figure S4, 0.1 < f < 10 Hz), confirming the soft solid-like nature of these hydrogels. By taking storage modulus from multiple runs at values $\varepsilon \approx 0.2\%$ and $f \approx 1$ Hz, we compared the storage modulus across all formulations and concluded that there were no statistical differences between any of them (Figure 2F). We noticed that peptide **YEF8** had the largest spread of storage modulus, correlating well to the observed cloudy-like bulk hydrogel state. The storage modulus of all SAPs falls in the range of 3.4 ± 2.8 kPa, broadly covering a range of acceptable biomechanical values for soft tissues,[52] indicating that any observed effects in cellular behavior between these sequences should not be directly linked to any difference in stiffness.

2.2. Molecular Dynamics Evaluations of SAPs. To obtain detailed atomistic insights into the structural stability and internal organization of SAPs, a series of MD simulations at atomistic resolution were conducted for individual peptide variants. For each SAP, free MD simulations starting from preassembled antiparallel β-sheet conformations demonstrated the stability of SAPs over 1 μs (Figure 3 and Supporting Movies S1, S2, S3, S4, and S5). Validation was based on an analysis of the secondary structure motifs of the SAP variants (Figure S5). The analysis indicated that most of the identified secondary structural motifs remained in an antiparallel β-sheet conformation with the tendency to retain this structure following the trend **YEF8Y** > **EYF8** > **EF8** > **YEF8** > **EF8Y** (Table S1). The greatest tendency to maintain an antiparallel

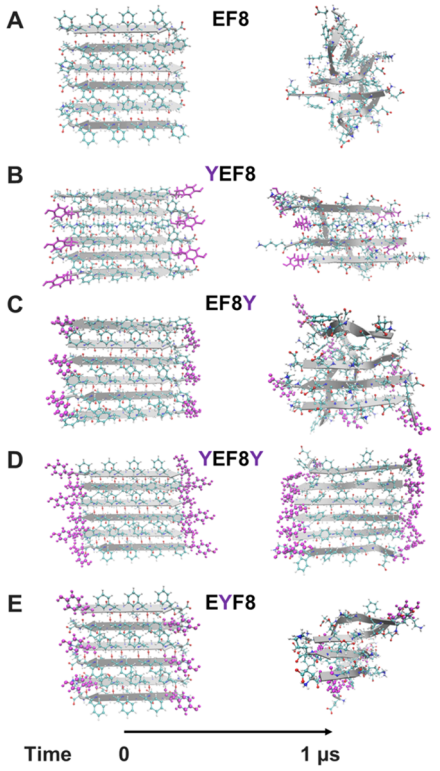

Figure 3. Snapshots of (A) **EF8**, (B) **YEF8**, (C) **EF8Y**, (D) **YEF8Y**, and (E) **EYF8** SAPs showing starting structures (left, time 0) and final structures (right) after 1 μs of MD simulation. The position of tyrosine residues is highlighted in magenta. Movies of full simulations are included as supporting material (SM1−SM5).

β-sheet structure was observed in the case of the **YEF8Y** variant (with 82.05% of preserved antiparallel β-sheet motive), suggesting that stabilization arises from the presence of tyrosine residues on both sides of the peptide fiber moieties. Although some individual fibers deviated (but not completely deflated) from the preassembled structure (with two fibers in the case of **EF8**, **YEF8**, **EF8Y**, and **EYF8**), they largely retained their β-sheet configuration (Table S1 and Figure S5). A small number of unstructured bends was observed, primarily at the terminal ends of the fibers exposed to solvent molecules. Strong internal organization was also evidenced by the robust network of hydrogen bonds between individual fibers (Figure S6). The data suggest a high propensity of SAPs to retain antiparallel β-sheets and conform with the presented FTIR, ThT binding assay, and CD spectroscopy data (Figures 2E and S2). Overall, experimental and computational data are indicative that all SAPs follow to a varying extent similar antiparallel β-sheet conformation at physiological pH.

2.3. Structural Assessment of SAPs by TEM, SEM, and SAXS. Nanofiber sizes and morphologies were characterized using TEM, SEM, and SAXS, all shown in Figure 4. TEM revealed entangled nanofibers and networks in all SAP hydrogels, consistent with the fibrillar structure for β-sheet-rich structures. **EF8** consisted of the thinnest nanofiber population with a diameter in the range of 10 nm, and some small population of larger rod-like objects (Figure 4A). Our previous work demonstrated that the thinnest nanofibers for **EF8** form in the range of 1.51 ± 0.43 nm;[41,41] however, we note this measurement was carried out on samples prepared directly in a solution form at 0.5 mM, rather than measured on

https://doi.org/10.1021/acsami.4c19900
ACS Appl. Mater. Interfaces 2025, 17, 27740−27758

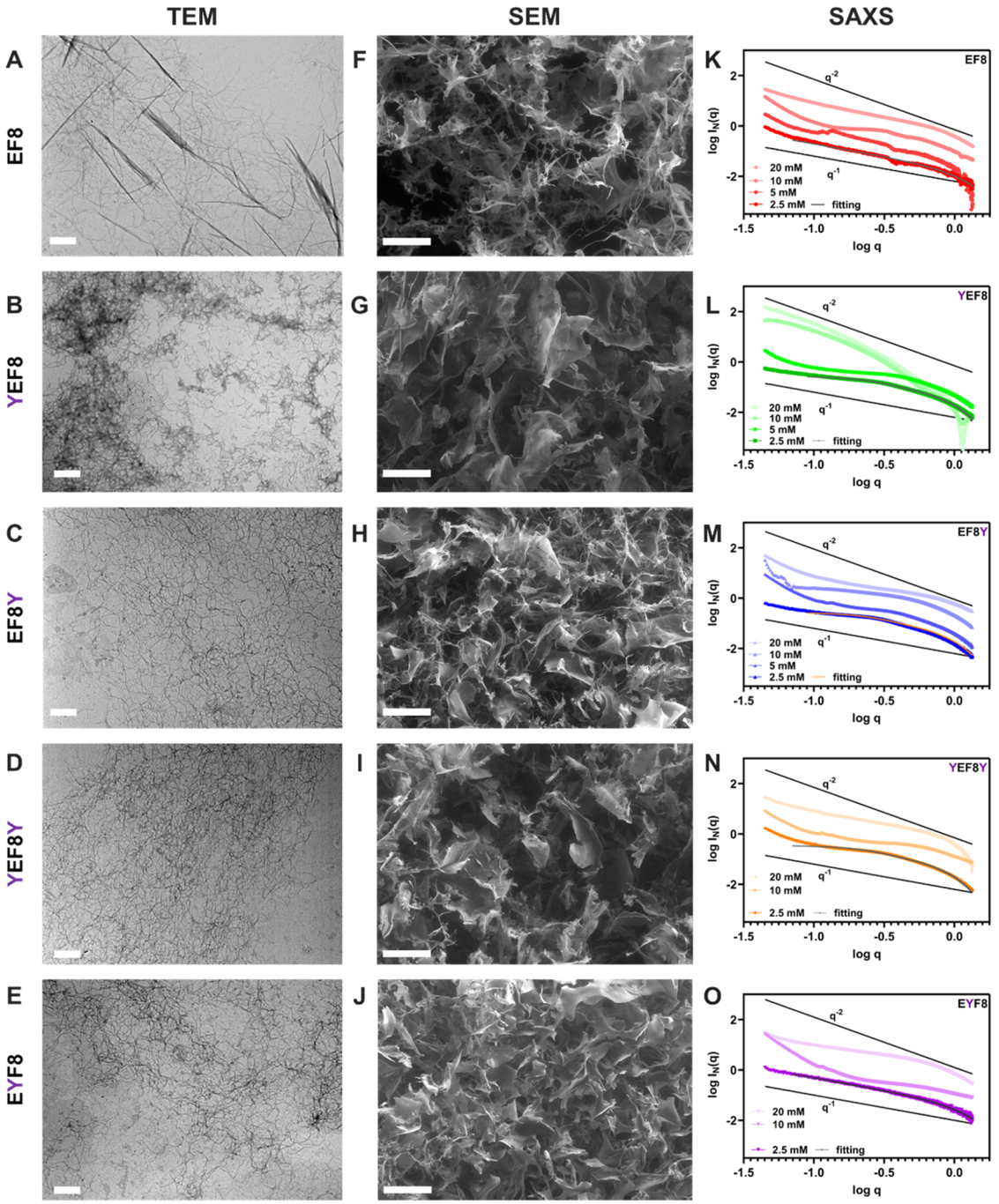

Figure 4. TEM (A–E) and SEM (F–J) images obtained for **EF8**, **YEF8**, **EF8Y**, **YEF8Y**, and **EYF8** (noted on the left-hand side for all rows). TEM images were obtained on 100-fold diluted hydrogels prepared originally at 20 mM concentration. TEM scale bars = 1 μm. SEM images were obtained on freeze-dried 20-fold diluted hydrogels in the variable pressure mode (for uncoated samples). SEM scale bars = 200 μm. (K–O) SAXS characterization of **EF8**, **YEF8**, **EF8Y**, **YEF8Y**, and **EYF8** SAPs/hydrogels prepared at different concentrations (2.5, 5, 10, and 20 mM) in the double logarithmic plot of $I_N(q)$ vs q representation. The straight lines depict the type of slope for easier visualization. In (N), the 5 mM **YEF8Y** sample was not measured properly during beamtime due to the Arinax sample change robot's failure to pick and load it up during automated measurements (based on the resulting spectra of an empty capillary). In part (O), 5 mM **EYF8** was the only sample for which consecutive radiation damage was noticed, hence it was excluded from the analysis/presentation. Each 2.5 mM curve in A–E has a corresponding cylindrical fitting curve fitted through (the used model is explained in detail in Section 2.4).

diluted bulk hydrogels like here. This sample preparation leads to observations of much thicker stacks of fibrillar bundles rather than individual smallest nanofibers. To confirm the 3D environment of a bulk hydrogel, we performed SEM imaging in variable pressure mode to avoid charging and coating artifacts (Figure 4F–J). We imaged freeze-dried samples both at 20 mM (×1) and 20-fold diluted (×20) to investigate the effects of possible interruption by the dilution effects (Figure S7). In a nondiluted state (Figure S7, ×**1**), all hydrogels displayed typical space with collapsed peptide structure and empty space in between. Only upon dilution, regions of nanofibers were observed (Figures 4F–J and S7). We acknowledge the

https://doi.org/10.1021/acsami.4c19900
ACS Appl. Mater. Interfaces 2025, 17, 27740–27758

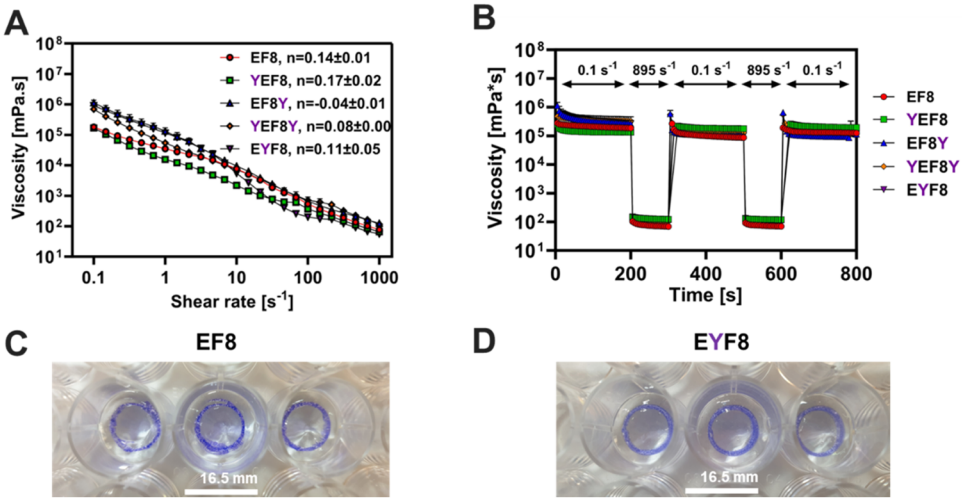

Figure 5. (A) Steady flow experiments at 37 °C of all SAP hydrogels prepared at 20 mM concentration. Flow index (n) calculated using eq 2 (see Section 4) is provided for each peptide after its name. Error bars (SD) are included for all samples (n = 2); however, they might not be visible due to their small size. (B) Rotational flow recovery experiments at 37 °C of all SAP hydrogels prepared at 20 mM concentration. An average of n = 2 is plotted, without error bars, as they would obscure the visibility of data. The used shear rate is plotted above each corresponding region. Digital photos of concentric circles printed into 3 neighboring wells with 20 mM SAPs ink of (C) **EF8** and (D) **EYF8** into Carbopol bath.

difficulty in utilizing this microscopy technique to elucidate the exact morphologies of SAP hydrogels but provide evidence of their general 3D morphology by SEM and of the types of nanostructured objects building them via TEM.

Considering TEM images, **YEF8** distinctly consisted of larger amounts of bundles of nanofibers (Figure 4B), whereas **EF8Y**, **YEF8Y**, and **EYF8** all formed well-defined thin-fibrillar networks (Figure 4C−E). The average widths ± SD of fiber and fiber bundle widths obtained from TEM are 41 ± 15, 73 ± 50, 37 ± 8, 36 ± 7, and 40 ± 8 nm for **EF8**, **YEF8**, **EF8Y**, **YEF8Y**, and **EYF8**, respectively (Figure S8). This indicates that the only statistically different sample compared with all other SAPs is **YEF8** (p < 0.001) (Figure S8). This might be indicative of a more pronounced tendency for **YEF8** peptide to form aggregated β-sheet bundles via lateral peptide stacking of β-sheet thin nanofibers, compared with thin networks observed for other SAPs. TEM suggests that the control sequence, **EF8**, has small tendency for this formation, although β-sheet thin nanofibers remain a prevalent self-assembled nanostructure, as previously observed.[41] Although TEM cannot conclusively discern secondary structures, the observed nanostructures are consistent with the formation of β-sheet-rich nanofibers. Here, we note different global rearrangements of final SAP structures noted in MD simulations (Figure 3), indicating limitations of computational technique to decipher differences on a larger spatial scale. Nevertheless, FTIR, ThT binding assays, and MDs all point to the fact that β-sheet structure is an underlying building block of nanostructures observed for SAPs in TEM. To note, we did not observe any significant morphological differences in SEM between our samples, with all qualitatively appearing similar at magnifications from 100× to 5000×.

We performed a structural analysis utilizing SAXS to confirm the presence of nanofibers and their dimensions for all SAPs. Figure 4K−O shows the SAXS patterns obtained for all SAPs at various concentrations in the range of 2.5−20 mM, presented as double logarithmic plots. For all samples prepared at 2.5 mM (on the border of CGC), a region of q^{-1} behavior, typical of the scattering of rod-like objects, can be observed.[53] For **EF8** and **EYF8**, the q^{-1} region extends for most of the q-range (Figure 4K,O). For all other SAPs, even at 2.5 mM, nonlinear curves were observed, with higher q regions following q^{-2} behavior, often associated with flat ribbons, lamella, or disc-shaped particles.[26] This indicates the formation of flattened structures in the order of 5−20 nm, in line with our TEM observations. The size of these ribbons shifts as the concentration increases for the **YEF8** sample toward the low q region (Figure 4M), indicative of the formation of larger rod-like or ribbon-like bundles, again matching well with the observed bundling of nanostructures in TEM. Furthermore, this indicates that the critical transition and associative bundling for **YEF8** occur above 5 mM concentration. For **EF8Y** and **YEF8Y** SAPs, the q^{-2} region persists in the order of 5−20 nm (higher q), confirming the structural built-up from individual nanofibers persists. To confirm this individual built-up of all SAPs, we attempted fitting a cylindrical model (see Section 2.4) to the obtained curves at 2.5 mM concentrations (Figure 4K−O). In all cases, omitting small aggregation regions at low q values, we obtained good fits of individual infinite-like cylinders with radius in the range of 1.9 ± 0.2 nm (diameters in the range of 3.8 ± 0.4 nm), in good agreement with the estimations for the nanofibers formed from this family of β-sheet SAPs[30,41] and our MD simulations.

All SAPs self-assembled into hydrogels above critical gelation concentration CGC ≈ 2.5 mM displayed characteristic high β-sheet content, similar built-up from individual nanofibers with d ≈ 3.8 ± 0.4 nm and larger associative flattened bundles in the range of 5−20 nm, similar storage modulus, except for **YEF8**, which retained slight cloudiness at physiological pH, had the largest spread in storage modulus values, and showed higher tendency for bundling above 20 nm size. Altogether, the results from Sections 2.1, 2.2, and 2.3 indicate that the addition of the tyrosine residues does not affect the overall ability of the peptides to form β-sheet nanofibers; however, it seems to affect the ability of these nanofibers to aggregate/associate and form larger fiber bundles, depending on the tyrosine position in the peptide sequence.

https://doi.org/10.1021/acsami.4c19900
ACS Appl. Mater. Interfaces 2025, 17, 27740−27758

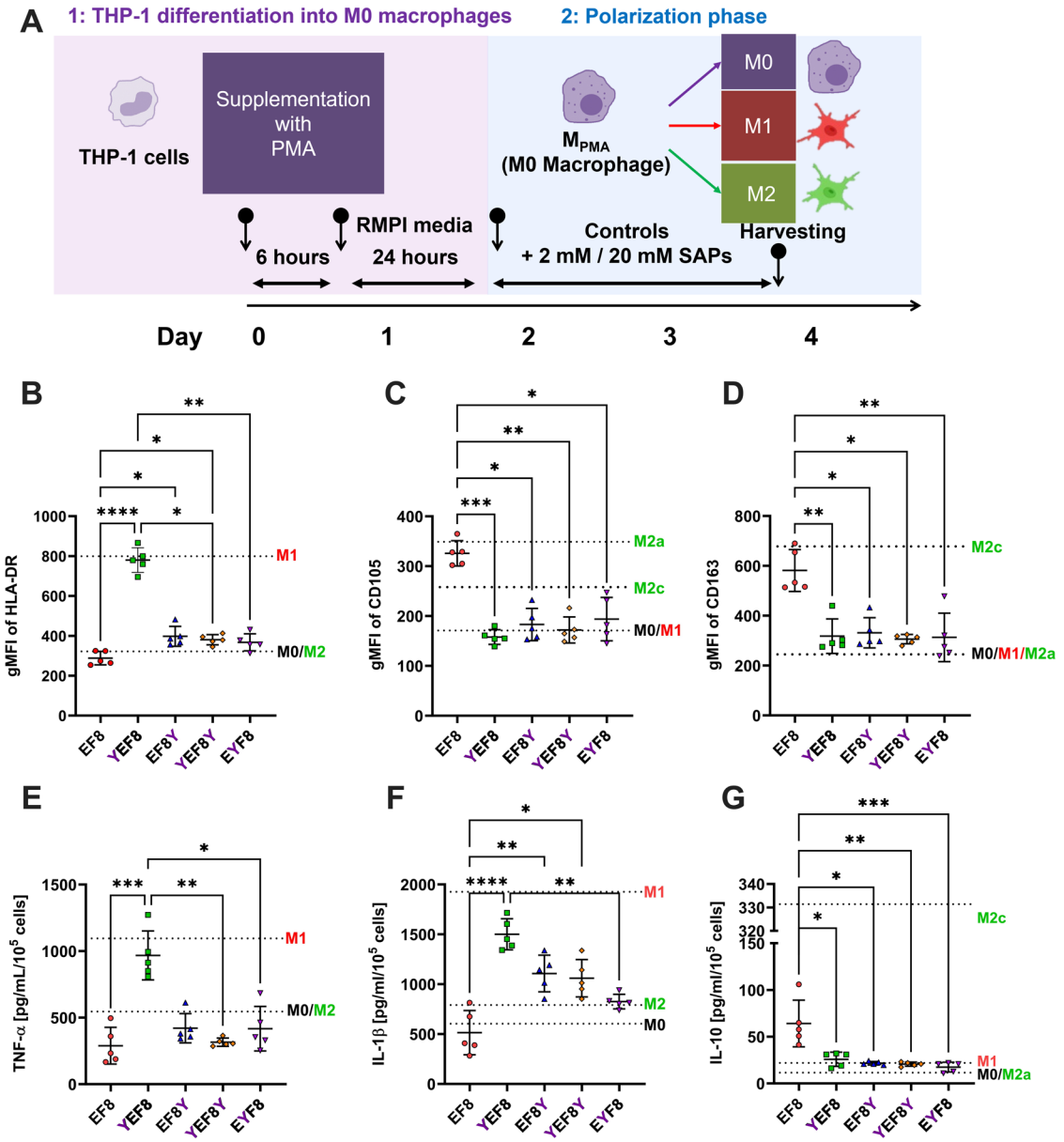

Figure 6. (A) Scheme summarizing the differentiation protocol of THP-1-derived MΦs. THP-1 cells were differentiated into M0 MΦs by treatment with 300 nM phorbol-12-myristate-13-acetate (PMA) for 6 h, followed by resting for 24 h in cell culture media. Subsequently, M0 MΦs were either cultured in the presence of the 2 mM SAPs (<CGC) supplemented in the cell culture medium for 48 h or detached and cultured on top of 20 mM SAP hydrogels. Quantitative analysis of cell surface markers of (B) HLA-DR, (C) CD105, and (D) CD163 for all 2 mM SAPs. Geometric mean fluorescence intensity (gMFI) was plotted. The black line and error bar in the plot represent mean and standard deviation, respectively. (E−G) Cytokine secretion profile using multiplex bead-based ELISA for all 2 mM SAPs. Significant changes were found only in 3 cytokines presented here: (E) TNF-α, (F) IL-1β, and (G) IL-10, for all SAPs. In all cases (B−G), horizontal dashed lines depict median values for the control MΦs with different polarization states obtained as indicated in the Section 4. Statistical analysis in B−G was done by the Kruskal−Wallis multiple comparisons test. Statistically significant results were considered for $p < 0.05$ (* - < 0.05, ** - < 0.01, *** - < 0.005, and **** - < 0.001).

2.4. Rheological Properties and Embedded 3D Printing of the SAP Inks. One key property of the developed SAP hydrogels is their injectability for minimally invasive surgery and use in biomedical additive manufacturing.[54,55] Therefore, we have measured viscosity curves and rotational flow recovery for all SAP hydrogels (hence named SAP inks in this section) at 20 mM concentration. Figure 5A shows the viscosity curves at 37 °C which were fitted to a power law model (eq 2, Section 4) to give shear-thinning exponents (n). All SAPs followed $n < 1$, indicating good downstream processability.[54] Flow recovery showed an immediate decrease of viscosity of about 3 orders of magnitude upon increase of shear rate, indicative of a transition to a low viscosity state (Figure 5B). This profile is indicative of increased extrudability or printability under the shear conditions present in the needle or nozzle. Upon cessation of the high shear conditions, representative of the material leaving the nozzle, the viscosity recovers to the same order of magnitude as the initial values, which is indicative of shape retention after extrusion. **YEF8** was the only SAP ink recovering more than 100% of its initial viscosity 40 s after cessation of the high shear (Figure 5B, green squares). The

https://doi.org/10.1021/acsami.4c19900
ACS Appl. Mater. Interfaces 2025, 17, 27740−27758

YEF8 SAP ink exhibited distinct behavior compared with all other SAPs, as evidenced by observations in TEM and its slight cloudiness in the gel form. The viscoelastic recovery of the tyrosine-containing SAP inks at the same 20 mM concentration was investigated also in oscillatory rheology, by applying low (0.2%) in alternation with high shear strain (100%) over 10 min intervals at a fixed frequency of 1 Hz (Figure S9A). **YEF8**, **EF8Y**, and **YEF8Y** behaved similarly to the previous case of **F8** peptide,[30] with a rather rapid and steady return to the original values. In this test, **EYF8** SAP ink did not recover after the first interval, which might be indicative of different network morphology or much longer relaxation processes in the network. The differences detected between oscillatory and flow recovery suggest also varying susceptibility of these types of materials to the type of applied shear.

Finally, to demonstrate the simple printability of our formulations, we selected the control SAP **EF8**, and one tyrosine-containing SAP, **EYF8**, and demonstrated their freeform 3D printing. In Figure 5C,D, inks were centrifuged at 1000 rcf for 5 min before printing, whereas in Figure S9B–C, were centrifuged at 3220 rcf for 5 min before printing. We noticed that in the case of longer centrifuging time, qualitatively assessed thinner rings were obtained for **EYF8** at the expense of higher variation and inconsistencies of the structure. Hence, final structures could be modulated by the preconditioning step of the SAP ink in the cartridge (Figures 5C,D and S9B–C). We chose a Carbopol-based microgel bath and ring-like circular structures as a simple model demonstrating that injectability and printing are possible, with good structural fidelity. Multiple dynamic factors impact printing outcome, including barrel and needle temperature, extrusion pressure, and head velocity.[54,55] Hydrogel physicochemical parameters can also influence printability, for example, varying peptide concentration or compositing will directly change the rheological properties.[56]

2.5. Immunological Effects Exerted on Genetically Similar Monocytic THP-1 Cells-Derived MΦs and SAPs Cytotoxicity. In the first instance, we decided to screen our family of SAPs prepared < CGC (at 2 mM, clear solutions) with genetically similar monocytic THP-1 cells. These cells enable rapid screening of the immunomodulatory potential by minimizing any biological variability stemming from primary human cells, thereby ensuring any differences between responses indeed come from the influence of SAPs. In the first instance, we directly tested whether SAPs have any capacity to activate NFκB signaling pathway, well correlated with the induction of pro-inflammatory responses,[57] directly on THP-1 monocytic cells with the NFκB-GFP reporter gene (Figure S10). None of SAPs triggered activation of this inflammatory pathway. This response was the same as the untreated control and cells treated with IFN-γ, which is known not to trigger this pathway. Across all tested samples, only when cells treated with TNF-α activated this pathway (Figure S10).[58] Based on the absence of obvious inflammatory response, we then aimed to confirm the general polarization capacity and tested it for all SAPs, both at 2 mM soluble nanofiber concentration (<CGC), as well as on the top of 20 mM hydrogels, against THP-1-derived MΦs following the protocol established by Sapudom et al. (Figure 6A).[59] First, we confirmed that SAPs were not cytotoxic by evaluation of the DRAQ7 in flow cytometry (see Section 4 for details). All SAPs, both in soluble 2 mM and in hydrogel form at 20 mM showed >90% of live cells (Figure S11).

Next, we confirmed the general cytotoxicity to both stromal cells utilizing L929 mouse fibroblasts and primary human fibroblasts. Lactate dehydrogenase (LDH) released into the medium after 24 h treatment with both supplemented 2 mM SAPs added to cell culture medium and for cells cultured directly on 20 mM hydrogels was measured and showed no significant differences between the constructs and the positive TCP control, with all levels lower than 15% (and 85% viability of cells retained) (Figure S12A). We also checked the metabolic activity of L929 cells and albeit noted much lower values for 2 mM SAPs, the cells cultured on 20 mM hydrogels had their metabolic activity retained (Figure S12B). The 2 mM supplementation of SAPs in medium lowered cell attachment compared with the cells seeded on the SAP hydrogels directly. This lower metabolic activity is expected as the developed SAPs do not contain any attachment/binding sites for stromal cells.

As an additional check, we supplemented 2 mM SAPs in cell culture medium to primary human fibroblasts and evaluated their cytotoxicity compared with TCP with or without TGFβ1 supplementation (Figure S12C,D). All supplemented SAPs led to the same number of cells as in the TCP-TGFβ1 control group (Figure S12C), indicating their lack of cytotoxic effects. We then measured the possible influence of 2 mM SAPs on the differentiation of fibroblasts into myofibroblasts using αSMA$^+$ positive cell counting and found no significant differences between TCP-TGFβ1 and SAPs groups (Figure S12C). As such, we briefly conclude that SAPs do not induce any cytotoxic effects on stromal cells.

2.5.1. Influence of Soluble SAPs at 2 mM (<CGC) on THP-1 Cells-Derived MΦs. MΦ phenotypes were then characterized for 2 mM SAPs using their specific surface markers, namely, HLA-DR for pro-inflammatory macrophages (M1) and CD105 for anti-inflammatory macrophages (M2) by flow cytometry.[10,38] We observed a significantly higher abundance of HLA-DR surface markers for cells supplemented with **YEF8** (Figure 6B), indicating its pro-inflammatory polarization capacity. On the other hand, we noticed a high abundance of CD105$^+$ cells when supplemented with control **EF8** SAP (Figure 6C), indicating cell polarization toward the M2 phenotype.[10] The obtained subtypes correspond well to the control M1 and M2 types, presented in all graphs as horizontal lines. Importantly, none of the other SAPs appeared to have significant expression of these cell surface markers and hence do not trigger any obvious pro- or anti-inflammatory response in this model, under the tested conditions. Given the importance of the M2 subtypes in tissue resolution, next we evaluated specific surface receptors, including CD206 and C163, known to be associated with M2a and M2c subtypes, respectively.[10] Interestingly, no significant differences were found for CD206 receptors between all SAPs (Figure S13A), whereas the highest abundance of CD163$^+$ was found when supplemented with **EF8** SAP (Figure 6D). This indicates that **EF8** peptide may stimulate the MΦs toward a tissue repair state, promoting the healthy restoration of normal architecture.[10,60]

We further studied the secretion profiles of 13 most common cytokines released by MΦs supplemented with 2 mM SAPs, using multiplex bead-based ELISA: IL-4, IL-2, CXCL10 (IP-10), IL-1β, TNF-α, CCL2 (MCP-1), IL-17A, IL-6, IL-10, IFN-γ, IL-12p70, CXCL8 (IL-8), and TGF-β1.

https://doi.org/10.1021/acsami.4c19900
ACS Appl. Mater. Interfaces 2025, 17, 27740−27758

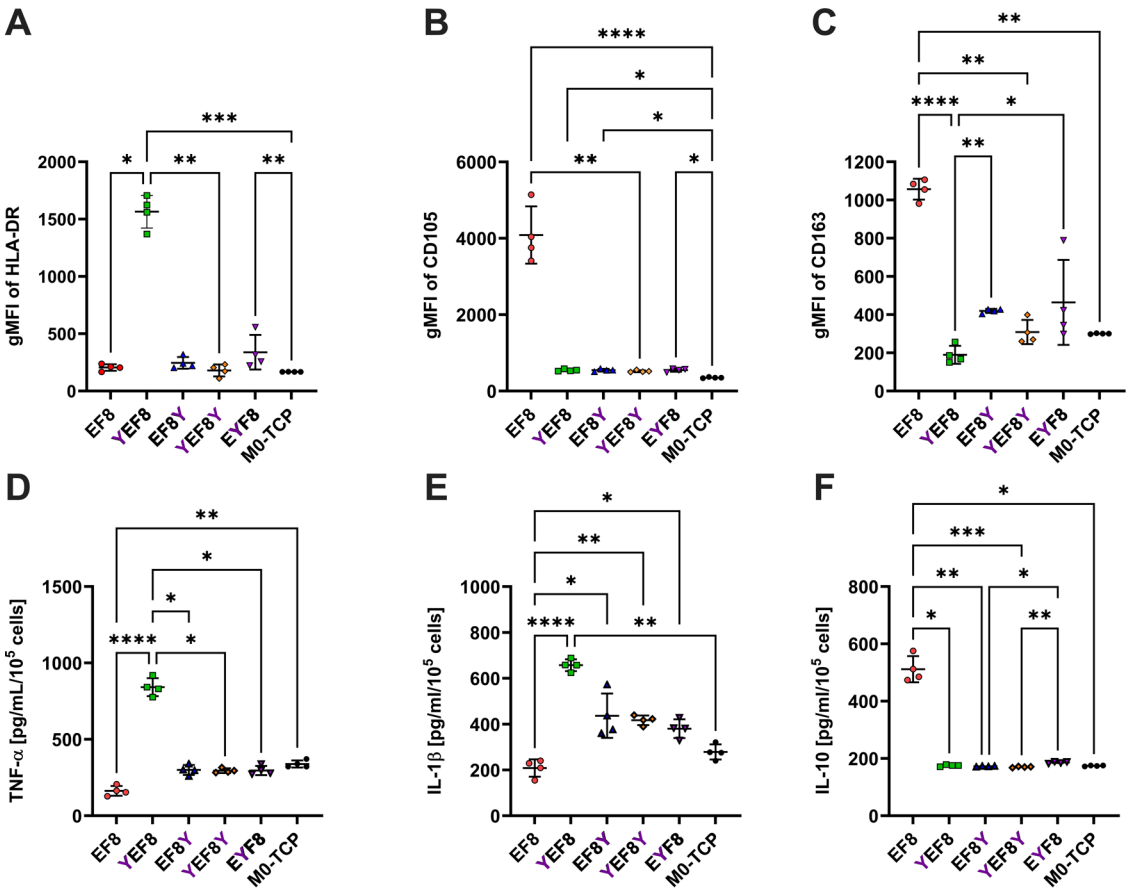

Figure 7. M0 THP-1-derived MΦs were cultured on the top of the 20 mM hydrogels for 48 h. Quantitative analysis of cell surface markers of (A) HLA-DR, (B) CD105, and (C) CD163 for all SAP hydrogels. Geometric mean fluorescence intensity (gMFI) was plotted. The black line and error bar in the plot represent mean and standard deviation, respectively. (D−F) Cytokine secretion profile using multiplex bead-based ELISA. Significant changes were found only in 3 cytokines presented here: (D) TNF-α, (E) IL-1β, and (F) IL-10. In all cases (A−G), horizontal dashed lines depict median values for the control MΦs with different polarization states obtained as indicated in the Section 4. Statistical analysis in B−G was done by the Kruskal−Wallis multiple comparisons test. Statistically significant results were considered for $p < 0.05$ (* - < 0.05, ** - < 0.01, *** - < 0.005, and **** - < 0.001).

Significant changes were found in three of the tested cytokines: pro-inflammatory—TNF-α (Figure 7E) and IL-1β (Figure 6F), and anti-inflammatory—IL-10 (Figure 6G). Again, **YEF8** SAP exhibited the largest amounts of released pro-inflammatory factors (TNF-α and IL-1β) compared with all other SAPs, and was similar in the level to control M1 (Figure 6E,F), confirming flow cytometry data. **YEF8Y** and **EYF8** SAPs had slightly elevated release of IL-1β compared with **EF8** ($p <$ 0.05); however, values were significantly lower compared with the control M1 (Figure 6F). No noticeable changes were seen in TNF-α expression (Figure 6E). **EF8** SAP induced the highest release of IL-10, an important cytokine for the remodeling of external matrix by MΦ, thus confirming polarization toward the M2c subtype.[10,61]

2.5.2. Influence of SAP Hydrogels at 20 mM on THP-1 Cells-Derived MΦs. Subsequently, we cultured M0 MΦ on 20 mM SAP hydrogels and evaluated their polarization phenotype using the same markers (HLA-DR, CD105, CD163, and CD206) by flow cytometry (Figures 7A−C and S13A,B). In all cases, we noticed the same polarization trend as in the case of supplemented 2 mM SAPs (Figure 6B−D), albeit with gMFI values significantly increased.

In ELISAs, the same trends were obtained in the secretion of TNF-α, IL-1β, and IL-10 for 20 mM SAP hydrogels (Figure 7D−E) as for 2 mM soluble SAPs (Figure 6E−G). However, unlike the 2 mM soluble SAPs case, in the case of 20 mM SAP hydrogels, we noticed significant differences in several other cytokines in our multiplex ELISA:

- pro-inflammatory: IFN-γ (Figure S14A), IP-10 (CXCL10) (Figure S14B), IL-8 (Figure S14C), and IL-12p70 (Figure S14D).
- regulatory: MCP-1 (Figure S14E) and IL-2 (Figure S14F).

Higher levels of IFN-γ, IP-10, IL-8, IL-12p70, and MCP-1 (Figure S14), along with TNF-α and IL-1β secretion (Figure 7D,E), suggest that **YEF8** supplementation indeed generated MΦs with pro-inflammatory phenotype and M1-like characteristics, as these cytokines are typically associated with pro-inflammatory responses and activation of M1 MΦs.

We also observed higher levels of IL-8 and IL-2 and lower levels of MCP-1 for **EF8** peptide, which original investigation suggested polarization toward an M2c phenotype. These levels suggest possible further activations in this atypical M2c phenotype, as IL-8 is involved in the activation of neutrophils and possible promotion of angiogenesis,[62] whereas IL-2 is generally associated with T-cell activation.[63] We also noted significantly low levels of MCP-1 for both **EF8** and **YEF8Y** peptides (Figure S14E), indicating these SAPs might reduce the recruitment of monocytes and move toward the natural

https://doi.org/10.1021/acsami.4c19900
ACS Appl. Mater. Interfaces 2025, 17, 27740−27758

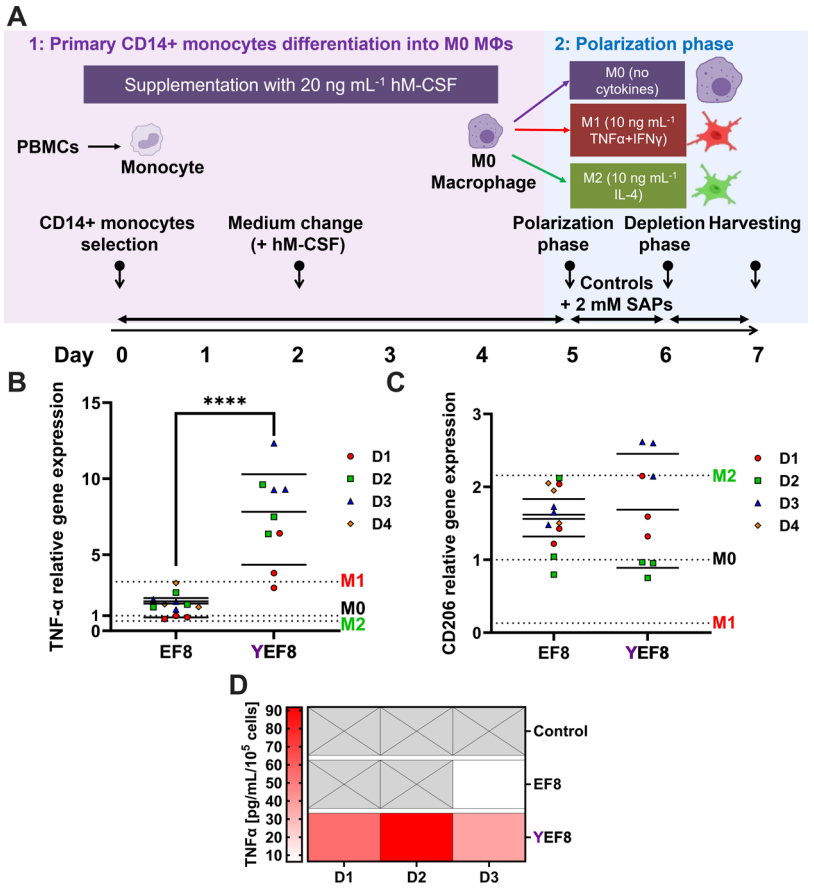

Figure 8. (A) Differentiation protocol and subsequent characterization of peripheral blood mononuclear cells (PBMCs)-derived MΦs. PBMCs were differentiated into M0 macrophages over 5 day period by supplementation with 20 ng mL^{-1} human macrophage colony-stimulating factor (hM-CSF). At day 5, differentiated M0 MΦs were polarized by medium supplemented with 10 ng mL^{-1} TNF-α and IFN-γ toward an M1 state (M1 control) and 10 ng mL^{-1} IL-4 toward an M2 state (M2 control) for 24 h, followed by a 24 h rest in medium without cytokines. Untreated M0 MΦs were treated as control samples and cultured in medium without any cytokines. The same three polarization states were maintained (M0, M1, M2), either without any external influence of materials (control) or in the presence of the 2 mM SAPs supplemented in the cell culture medium at day 5 (for 24 h). Gene expression of (B) TNF-α and (C) MRC1 (CD206) measured by RT-qPCR for untreated MΦs supplemented with 2 mM of **EF8** or **YEF8** SAPs. Gene expression is represented as fold change compared with RPLP0 (a housekeeping gene) of the M0 untreated control group per each donor ($n = 3$). Horizontal dashed lines depict average values across all donors for the control MΦs with different polarization states. Analysis by two-way ANOVA with Tukey's multiple comparisons test. Statistically significant results were considered for $p < 0.05$ (* - < 0.05, ** - < 0.01, *** - < 0.005, and **** - < 0.001). (D) TNF-α secretion measured by ELISA for cells treated with 2 mM SAPs (represented in rows) with the same conditioning as described in part D. Gray crossed boxes indicate measurements below the limit of detection.

progression of the reparative state. The obtained cytokine profiles for **EF8** SAP suggest possibly a mixed phenotype with characteristics of both M1 and many M2 MΦs subphenotypes, with most of the data pointing toward M2c being a predominant state.

The final MΦ fate is driven by the complex interplay between external environmental signals and hardwired differentiation programming capabilities. Given the observed opposed functional polarization states of MΦ between **EF8** (M2c) and **YEF8** (M1) SAPs, we hypothesize that the underlying edge-driven chemical moieties could be responsible for the initiation of this function, as demonstrated in previous sections. The role of viscoelasticity of bulk hydrogels in the overall modulation does not seem apparent, as here we observed matching profiles for both the soluble nanostructures at a concentration of 2 mM (<CGC) and 20 mM hydrogels. Wang and Bratlie provided guidelines for MΦ polarization as a function of used polymer chemistry properties.[64] They argued that chemistry leading to more H-bonding capacity and higher hydrophilicity stimulates MΦ toward the M1 state, whereas overall charge plays a role in M2 modulation. Our findings suggest that in the case of **YEF8** SAP, in principle, the tyrosine placed in the first position may enable additional H-bonding and contribute to the polarization of the M1 state compared with **EF8** (Figure S6A,B). However, noticing lack of such induction for other Y-containing SAPs (Figure S6C−E) seems to indicate the other factors, such as the unique chemical arrangement of amino acids in this SAP or associative bundling behavior as the putatively prevalent factor in this polarization.

2.6. Immunological Effects Exerted on Clinically Relevant PMBC-Derived MΦs. Next, to confirm and assess clinical viability of the unique polarization capacity of **EF8** and **YEF8** SAPs, we used an established protocol of peripheral blood mononuclear cells (PBMCs)-derived MΦs[38] (Figure 8A) from 5 human donors and evaluated TNF-α/CD206 gene expression (Figures 6B,C and S15A,B) and released TNF-α cytokine (Figures 8D and S15C). As expected, averaging from all donors, TNF-α was typically upregulated in M1 control and downregulated in M2 control (Figures 8B and S15A), whereas CD206 was downregulated in M1 control and upregulated in

https://doi.org/10.1021/acsami.4c19900
ACS Appl. Mater. Interfaces 2025, 17, 27740−27758

M2 control (Figures 8C and S15B). When using primary cells, variation across donors is standard.[65,66] Patient-derived cells bring in a huge variety of environmental and genetic factors, including gender, lifestyle, cholesterol levels, and comorbidities to name a few.[67] Despite these challenges, data from primary cells increase the clinical relevance of our findings. Therefore, within the experimental variations, the overall results confirm previous observations, i.e., the upregulation of TNF-α (Figure 8B) and downregulation of CD206 in 2 donors in the M2 tested group (Figure S15B) for **YEF8** SAP. This also correlated well with the elevated levels of TNF-α detected almost exclusively for **YEF8** SAP (Figures 8D and S15C). Gray boxes in Figure 8D indicate that levels of TNF-α were below the limit of detection.

In general, for the **EF8** SAP, we observed most of the measurements falling closer to M0 control in TNF-α gene expression (Figures 8B and S15A) and a slight tendency toward M2 in CD206 gene expression (Figures 8C and S15B). No noticeable expression of TNF-α was observed in ELISA measurements for this SAP (Figures 8D and S15C). These results confirm the phenotype of THP-1-derived MΦs in Section 2.4 holds true for MΦs directly differentiated from PBMCs across multiple tested donors and brings a critical role of the **EF8** sequence as a possible orchestrator balancing repair of tissues, such as in wound healing[10] or tendon repair.[68] In general, two other tested SAPs, **EF8Y** and **EYF8**, showed downregulation of TNF-α (Figure S15A) and upregulation of CD206 (Figure S15B) in M0 groups, indicating possible MΦs polarization toward M2a-like state. Although this observation contrasts THP-1 cells-derived MΦs behavior in Section 2.4 and potentially depicts differences between the two types of cell sources, the conclusions from these two studies still indicate that these SAPs do not induce any significant inflammatory response compared with the **YEF8.** Unfortunately, the effects of **YEF8Y** SAP could not be evaluated due to the noticed interference of this SAP with the RNA extraction process. Nevertheless, the secreted TNF-α protein levels for **EF8Y**, **EYF8**, and **YEF8Y** were virtually negligible (Figure S15C), confirming the lack of pro-inflammatory response from these SAPs in this model.

3. CONCLUSIONS

In this work, we designed five β-sheet forming self-assembling peptide sequences: EFEFKFEFK (**EF8**), **Y**EFEFKFEFK (**YEF8**), EFEFKFEFK**Y** (**EF8Y**), **Y**EFEFKFEFK**Y** (**YEF8Y**), and E**Y**EFKFEFK (**EYF8**) (F: phenylalanine; E: glutamic acid; K: lysine, **Y**: tyrosine). We then investigated the role of repositioning the tyrosine residue on the self-assembly, gelation, and immunological function of macrophages derived from two discrete cell sources. Our results showed that the addition of tyrosine did not affect the ability of the peptides to form β-sheet-rich nanofibers. Titrations of peptides revealed that all SAPs carry a charge in the range of $-2 \leq Z \leq -1$ at physiological pH (7.2 ± 0.2), with close ζ-potential values in the range of −27.1 to −35.9 mV for all SAPs, and all forming self-supporting hydrogels above similar CGC ∼ 2.5 mM. The only exception was **YEF8**, which retained slight cloudiness at this pH when bulk hydrogels were formed. Furthermore, in bulk hydrogel form at 20 mM, all SAP hydrogels were characterized by similar storage modulus profiles in the range of 3.4 ± 2.8 kPa and were shear-thinning. We demonstrated SAPs **EF8** and **EYF8** SAP hydrogels were freeform 3D printable in an embedded bath, providing a preliminary assessment of the possible biofabrication routes for this class of SAP hydrogels. All SAPs self-assembled into thin nanofibers $d \approx 3.8 \pm 0.4$ nm, with **YEF8** and **EF8** demonstrating some propensity for associative bundling. **YEF8** was characterized by larger variability in storage modulus, which may be due to the presence of microscopic phase inhomogeneity, correlating well with larger nanostructure bundling observed in TEM. These SAPs displayed a good correlation with the response observed in MΦs derived from genetically similar monocytic model THP-1 cells and genetically variable peripheral blood mononuclear cells (PBMCs) from multiple donors. The presence of soluble **EF8** nanofibers (at 2 mM) induced a strong anti-inflammatory response and polarization toward M2a and M2c MΦ states, indicating this SAP as a possible modulator of the tissue repair. **YEF8** SAP (at 2 mM, solution state) displayed tendency for inducing strong pro-inflammatory response and polarization toward M1 MΦ phenotype, whereas **EF8Y**, **YEF8Y**, and **EYF8** SAPs did not induce strong inflammatory responses in our models. The same polarization effects were observed for THP-1-derived MΦ cultured on top of 20 mM SAP hydrogels, albeit inducing stronger expressions of HLA-DR, CD105, and CD163 receptors for the same polarizing peptides (**EF8** and **YEF8**). Since immunomodulation toward a certain state offers the opportunity to enhance functional recovery, here we provide a family of SAPs that can be used as nanobiomaterial immunomodulators. By minor variation of the position of tyrosine in the sequence, nanostructures with a tendency toward anti-inflammatory, pro-inflammatory, or nonimmunogenic polarization of MΦs were designed. At higher concentrations suitable for gel formation, caution should be exercised when correlating nanostructure and biological response, due to potential changes in phase behavior, as reflected in the nontransparency of **YEF8** at high concentrations. These responses seem to be linked to the types of nanostructures formed, as well as possible H-bonding edge-interactions stemming from the edges of these nanostructures or to a unique chemical arrangement of this SAP. There are reports that this family of SAPs can be uptaken by cells,[69] and thus one of the alternative polarization mechanisms might involve internal signaling after endocytosis of the peptide. However, deciphering the exact mechanisms of this polarization remains to be investigated in future studies, such as transcriptomics or proteomics. Our work brings basic physicochemical rules for the design of future immunomodulatory SAP nanobiomaterials and injectable hydrogels that could be used for reprogramming of immune system toward desired reparative or inflammation-induced states.

4. MATERIALS AND METHODS

4.1. Materials. Peptides were purchased as HCl salts from Biomatik Corporation (Wilmington, DE, Canada) and used as received. The peptide sequence purity was confirmed using reverse-phase high-performance liquid chromatography (HPLC) and was >92%. All solvents and reagents were purchased from Sigma-Aldrich and used as received.

4.2. Theoretical Charge and Experimental Titrations. The theoretical net charge of different peptide sequences at each pH value was calculated by the following equation

$$Z = \sum_i N_i \frac{10^{pK_{a_i}}}{10^{pH} + 10^{pK_{a_i}}} - \sum_j N_j \frac{10^{pH}}{10^{pH} + 10^{pK_{a_j}}} \quad (1)$$

https://doi.org/10.1021/acsami.4c19900
ACS Appl. Mater. Interfaces 2025, 17, 27740−27758

where $N_{i/j}$ are the numbers of functional groups present on the peptide, and $pK_{ai/j}$ the pK_a are the basic ($i - pK_a > 7$) and acidic ($j - pK_a < 7$) values, respectively.[18] Peptide titration experiments were performed by the addition of a 0.05 M NaOH solution in 5 μL steps to a 1 mL of miliQ water (H_2O) peptide solution with an ~1 mM starting peptide concentration. After each NaOH addition, the samples were vigorously agitated using a vortexer to ensure homogeneous mixing and the pH was measured using an 827 Metrohm pH Meter (Metrohm AG, Switzerland). The experiments were repeated at least 2 times.

4.3. Hydrogel Preparation. Typically, for the preparation of 1 mL volume of the 20 mM hydrogel, the required amount of peptide powder was first dissolved in 700 μL of miliQ H_2O. To ensure full and homogeneous dissolution, the samples were then sonicated at 80 kHz for 30 min in an ice bath (to ensure low temperature). Hydrogels were then prepared by adjusting the pH of the peptide solutions to the desired value through the stepwise addition of a 0.5 M NaOH solution. After each addition, the samples were vigorously agitated using a vortexer to ensure homogeneous mixing. If bubbles were present after mixing, gentle centrifugation (at 4000 rpm for 1 min) was used to remove them. Concentrations and volumes were scaled as needed for each experiment.

4.4. Zeta-Potential (ζ) Measurements. The ζ of SAPs was measured at 37 °C and pH 7 using a Litesizer DLS 500 instrument (Anton Paar). 20 mM SAP hydrogels were diluted to 0.02 mM concentration using miliQ H_2O and sonicated for 30 min on ice. The final sample pH was adjusted by titration with 0.05 M NaOH or 0.05 M HCl to reach 7.1 ± 0.2. The measurements were repeated 3 times on 2 independently prepared replicate samples to ensure reproducibility.

4.5. Attenuated Total Reflectance–Fourier Transform Infrared (ATR-FTIR) Spectroscopy. Hydrogels or solutions were spread as prepared onto the crystal surface of a Bruker Tensor 27 spectrometer equipped with a diamond multibounce attenuated total reflectance (ATR) plate. The transmittance spectra were recorded (256 scans) between 4000 and 400 cm^{-1} with a resolution of 2 cm^{-1}. MiliQ H_2O was used as background and was automatically subtracted from the recorded spectra using the OPUS software provided with the instrument.

4.6. Fluorescence Thioflavin T (ThT) Assay. ThT was mixed in 20 mM of both peptide solutions/hydrogels during their preparation with a final 5 μM concentration. ThT assay was measured on an Infinite 200 Pro plate reader (Tecan, Männedorf, Switzerland). Excitation wavelength was set as λ_{exc} = 400 nm, and the fluorescence scan range was measured in the range of 460–600 nm. Pure ThT at 5 μM concentration was used as a background and subtracted from all measured peptide signals.

4.7. Circular Dichroism (CD) Spectroscopy. Samples were prepared by diluting hydrogels (100-fold) to 0.2 mM concentration in MiliQ water. After dilution, samples were vortexed for 60 s and sonicated on ice for 30 min. Subsequently, solutions were gently pipetted into a 1 mm optical path length quartz cuvette (Hellma). Samples were then scanned using a ChiraScan, Applied Photophysics, where spectra were recorded at a wavelength in the range of 180–280 nm with 1 nm step size, 0.5 s response time at 25 °C. Fresh miliQ water background was taken prior to each measurement and automatically subtracted from the data. The ellipticity data were then acquired in mdeg and are presented in the original unit. Spectra are shown from 180 to 260 nm as average from 5 measurements. Deconvolution of the CD spectra was done using the freely available DichroWeb (http://dichroweb.cryst.bbk.ac.uk/html/home.shtml) toolkit.[70] For deconvolution presented in Figure S2D, we used the self-consistent method (**SELCON3**) with reference data set in the range from 190 to 240 nm.[49,50]

4.8. Rotational and Oscillatory Rheology. Rheological studies were carried out on an Anton Paar MCR-302 rheometer (Anton Paar GmbH, Austria). All measurements were taken with a gap size of 0.5 mm and a parallel plate with a diameter of 25 mm. Samples were prepared as described above. Hydrogels were gently spread onto the rheometer's static bottom plate and the rheometer top plate was lowered to the desired gap size. To prevent sample drying during the measurements, silicone oil was applied around the plate to seal the hydrogel. Samples were left to equilibrate for 180 s and then frequency sweeps were assessed at a temperature of 37 °C, with a strain of ε = 0.2%. Amplitude sweeps were performed in an oscillatory mode at a constant frequency of f = 1 Hz at 37 °C, with strain varied from 0.01 to 1000%. All viscosity–shear rate experiments (flow curves) were performed at 37 °C, with samples subjected to shear rate from 0.01 to 1000 s^{-1}, and being held at each shear rate until a stable reading was reported by the instrument. The shear-thinning behavior was characterized by fitting the Power Law eq 1 to the linear region of the shear rate–viscosity rheology plot.

$$\eta = K\dot{\gamma}^{n-1} \tag{2}$$

where η is the viscosity, $\dot{\gamma}$ is the shear rate, K is the consistency value, and n is the shear-thinning exponent. Flow recovery tests in a rotational mode were performed by initially subjecting the sample to shear close to a zero-shear value (0.01 s^{-1}) for 200 s. Then shear rate was increased to 895 s^{-1} and kept for 100 s. Recovery was then monitored for 200 s by switching the shear rate back to 0.01 s^{-1}, and the same cycle was repeated. The oscillatory recovery experiments were performed by applying sequentially low (0.2%) and high shear strain (100%) in 10 min intervals over 2 cycles. All recovery tests were performed at 37 °C. All measurements were repeated at least two times, and average and standard deviation were presented.

4.9. Molecular Dynamics (MD) Simulations. Model systems of all peptide variants (**EF8**, **YEF8**, **EF8Y**, **YEF8Y**, and **EYF8**) were studied by means of molecular dynamics simulations. Initial structures of single peptide chains were built using the Fab tool implemented in PyMOL (ver. 2.5.5) software.[71] The protonation states of all peptides correspond to pH 7, with the C- and N-termini, as well as the charged polar amino acids (K, E), in their ionized forms. Subsequently, all peptide variants were preassembled along the fiber axis as single ladders in antiparallel β-sheets conformation, each composed of six individual peptides (see Figure 3). Resulted preassembled structures were placed into cubic box of 8 × 8 × 8 nm^3. All molecular dynamics simulations were performed using AMBER22 simulations software.[72] Parameters for peptides were described using Amber ff19SB.[73] Systems were solvated with OPC water model[74] and Li-Merz ions[75] were added to maintain the electroneutrality of systems. Prior to the production run, each system was subjected to energy minimization followed by a short 10 ns NpT simulation to equilibrate the box. The final production run was conducted in the NVT ensemble, with each simulation time set to 1 μs and time step of 2 fs. The temperature was kept constant at 298 K using weak-coupling algorithm[76] and the temperature coupling constant was set to 0.2 ps. The SHAKE algorithm[77] was used to constrain all bonds including hydrogen atoms. A cutoff of 1.0 nm was used for the Lennard–Jones interaction and the short-range electrostatic interactions. Long-range electrostatics was treated by Particle Mesh Ewald (PME) summation.[78] Periodic boundary conditions were applied in all directions.

4.10. Transmission Electron Microscopy (TEM). Peptide hydrogels were prepared at 20 mM concentration as described above and diluted 100-fold using deionized H_2O. The samples were then gently pipetted up and down for 60 s, followed by 60 s vortexing and sonication at 35 kHz at room temperature in normal mode for 3 min. A carbon film-coated 300 Mesh copper grid (Electron Microscopy Sciences, CF300-CU-50) was placed sequentially on a 10 μL sample droplet for 60 s. The sample was then blotted and a 10 μL droplet of Uranyless solution was applied for 60 s, blotted, and then rinsed using H_2O until finally left to dry for 5 min. TEM images were taken using a Hitachi TEM H800 transmission electron microscope running at 100 keV. A minimum of 100 nanofibers and nanofiber bundle widths were measured manually using ImageJ software for each SAP.

4.11. Scanning Electron Microscopy (SEM). Peptide hydrogels were prepared at 20 mM concentration as described above and diluted 20-fold using deionized H_2O. These were noted as ×1 and ×20 in names, respectively. All samples were then flash-frozen at −70 °C and lyophilized to form freeze-dried porous solids. These were

https://doi.org/10.1021/acsami.4c19900
ACS Appl. Mater. Interfaces 2025, 17, 27740–27758

carefully cut into disks and prepared on a multi-sample holder using carbon tapes for fixing. The samples were transferred via an airlock into the SEM chamber of the Hitachi field emission scanning electron microscope SU8700. They were then imaged at an accelerating voltage of 10 kV, at a recording speed of 20−40 s, a probe current of 107 pA, and a variable pressure between 45 and 50 Pa, using a BSE-signal (PDBSE, Photo Diode BSE) detector and an SE-signal (UVD, Ultra Variable Pressure) detector.

4.12. Small-Angle X-ray Scattering. SAXS experiments were performed on beamline B21 at the diamond light source (DLS) synchrotron (Didcot, U.K.), following the setup previously described.[79,80] Briefly, the energy of the beam was 13.05 keV, corresponding to an X-ray wavelength of 0.95 Å. The sample-to-detector distance was fixed to 3.7 m corresponding to an accessible momentum transfer vector range of 0.03 $nm^{-1} < q = (4\pi/\lambda)\sin(\theta/2) < 3.4$ nm^{-1}, where θ is the scattering angle and λ is the wavelength of the incident photons. Calibration of the SAXS detector (Eiger 4M, Dectris, Switzerland) was performed using silver behenate powder. Samples were collected at 20 °C for 20 consecutive framers at the exposure time of 1 s each. The samples were prepared as described above at 20 mM and subsequently diluted to lower concentrations of 10, 5, and 2.5 mM prior to measurements. pH was checked after each dilution to ensure the original pH was unaffected by the dilution process. Such prepared hydrogels were left on the agitator for 4 h at room temperature to ensure complete homogeneity. Samples were measured either in an empty Kapton tape or in quartz capillaries (1.5 mm outer diameter and 0.01 mm wall thickness) from Capillary Tube Supplies Ltd. (Bodmin, U.K.). These were, respectively, for Kapton tapes, used as background; they were subtracted from all spectra and data were reduced using ScatterIV (Rambo, R. P.). For samples placed in capillaries, an empty capillary was used as the background and subtracted from all spectra, and data were reduced using the Dawn software suite available from DLS. The 2D scattering patterns were integrated using azimuthal integration to generate the 1D scattering patterns. SAXS data were fitted using SasView 5.0.6 software (http://www.sasview.org/). The form factor used to fit this data was the cylinder model in SaSView (https://www.sasview.org/docs/user/models/cylinder.htm), which is a circular cylinder with uniform scattering length density. The scattering intensity of orientated cylinders is given by the model

$$I(q, \alpha) = \frac{\text{scale}}{V} F^2(q, \alpha) + BG \tag{3}$$

where $F(q, \alpha)$ can be defined as

$$F(q, \alpha) = 2(\Delta p)V \frac{\sin\left(\frac{1}{2}qL\cos\alpha\right)}{\frac{1}{2}qL\cos\alpha} \frac{J_1(qR\sin\alpha)}{qR\sin\alpha} \tag{4}$$

where V is the volume of the cylinder ($V = \pi R^2 L$, R = radius, L = Length), Δp is the contrast, thus is the scattering length density difference between the object that is scattering and the solvent, α is the angle between the axis of the cylinder and vector q, and J_1 is the first order of the Bessel function.

For randomly orientated particles in a SAXS experiment

$$P(q) = F^2(q) = \int_0^{\pi/2} F^2(q, \alpha)\sin(\alpha)\mathrm{d}\alpha \tag{5}$$

Therefore, the output of the one-dimensional scattering of randomly orientated cylinders can be given by

$$I(q) = \frac{\text{scale}}{V} \int_0^{\pi/2} F^2(q, \alpha)\sin(\alpha)\mathrm{d}\alpha + BG \tag{6}$$

The second virial coefficient for the cylinder is calculated based on the length and radius values and is used as the effective radius.

The 5 mM **YEF8Y** sample was not measured properly during beamtime due to the Arinax sample change robot's failure to pick and load it up during automated measurements (based on the resulting spectra of an empty capillary). Hence, we could not analyze this concentration in the analysis provided in Section 4.2. 5 mM **EYF8** was the only sample for which consecutive radiation damage was noticed, hence it was excluded from the analysis/presentation.

4.13. Freeform 3D printing. For embedded printing, we prepared a microgel bath from 0.8% (w/v) Carbopol 940 (Acros Organics Geel, Belgium) printing bath following previous protocols.[81] Briefly, 0.20 g of Carbopol 940 was dissolved in 20 mL of MiliQ H_2O and prior to printing, the pH of the bath was adjusted to 7.2 ± 0.2 with 2 M sodium hydroxide (NaOH). The Carbopol bath was stored at 4 °C until printing. One mL of bath per well was deposited into 24-well plates and degassed using an Eppendorf centrifuge at 500g for 5 min. Freeform 3D printing was then performed using a 3D Discovery Printer and BioCAD software (version 1.1−12) from RegenHu Ltd. (Villaz-St-Pierre, Switzerland) using a 20G needle with PTFE-with 0.61 mm (Nordson EFD, Westlake). 3 mL of SAP hydrogels **EF8** and **EYF8** were prepared at 20 mM concentration prior to printing as per the procedure above, with the addition of 20 μL of 10 mg mL^{-1} Coomassie Brilliant Blue R250 dye to enable easier visualization of printed structures. SAP inks were loaded into 3 cm^3 printing cartridges, which were either centrifuged at 1000 rcf for 5 min before printing (presented in Figure 5C,D) or centrifuged at 3220 rcf for 5 min before printing (presented in Figure S9B,C). SAP inks were deposited at a height of 2 mm above the bottom inside the Carbopol bath at a velocity of 0.5 mm s^{-1} and with a pressure of 0.5−1 bar. The printed structures were 3 circles vertically spaced by 1 mm in 3 separate wells. Printing was done at 23−25 °C range of ambient temperature and 12−25% relative humidity.

4.14. L929 Cells Culture. L929 mouse fibroblasts (Sigma-Aldrich, catalogue 85011425) were cultured in Dulbecco's modified Eagle's medium (DMEM, Gibco) supplemented with 10% v/v fetal bovine serum (FBS, Corning), 1% v/v Pen-Strep (100 U mL^{-1} of penicillin, 100 μg mL^{-1} of streptomycin, Gibco). The medium was changed every second day and cells were passaged until 80% confluency. Cells at passage 24 were used for all cell culture experiments.

4.15. L929 Cells Metabolic Activity. The metabolic activity of L929 cells was assessed using the CellTiter-Blue Cell Viability Assay (Promega, Dübendorf, Switzerland). 10,000 cells per well were cultured either on SAPs peptide hydrogels prepared at 20 mM and casted in the wells, or with 2 mM SAPs supplemented within the culture medium, for 24 h. A mixture of CellTiter-Blue Reagent and DMEM Low Glucose cell culture medium at a 1:5 (v/v) ratio was added to each well containing the gels at the 24 h time point. The fluorescence intensity of the samples was measured at 560Ex/590Em using the Infinite 200 Pro plate reader (Tecan, Männedorf, Switzerland) after transferring the reagent-media mixture to a 96-well plate. The medium placed on hydrogel samples without any cells for 24 h and 2 mM SAPs supplemented within the culture medium were used as blank measurements. These were subtracted from the readings taken with cells for respective samples.

4.16. L929 Cells Cytotoxicity. The amount of lactate dehydrogenase (LDH) released into the cell culture supernatant, indicating damage to the cellular plasma membrane, was measured using the Cytotoxicity Detection KitPLUS LDH (Roche, Sigma-Aldrich), following the manufacturer's protocol. In brief, supernatants of L929 cells cultured on hydrogels and with supplementation of 2 mM SAPs as described above were collected at the 24 h time point and centrifuged at 300g for 5 min at +4 °C. A 100 μL sample from each supernatant was transferred to 96-well plates, followed by the addition of 100 μL of working solution to each well. The plates were incubated for 30 min at room temperature. After adding 50 μL of stop solution, absorbance values were measured at 490 nm using the Infinite 200 Pro plate reader (Tecan, Männedorf, Switzerland). The percentage of cytotoxicity was calculated for each sample using the formula provided below

$$\text{cytotoxicity}(\%) = \frac{(\text{experimental value} - \text{low control})}{(\text{high control} - \text{low control})} \times 100\% \tag{7}$$

https://doi.org/10.1021/acsami.4c19900
ACS Appl. Mater. Interfaces 2025, 17, 27740−27758

The low control value was determined using the medium from cells cultured on plates at t = 30 min, while the high control value was obtained from the medium of cells treated with 9% Triton X-100 at 24 h.

4.17. Human Fibroblast Culture, Cytotoxicity, and Myofibroblast Differentiation. A total of 1.5×10^4 primary human fibroblasts (ATCC, Manassas, VA) were cultured in DMEM supplemented with 10% fetal bovine serum (FBS) and 1% penicillin/streptomycin (Gibco, Thermo Fisher Scientific, Inc., Dreieich, Germany), with or without 2 mM SAP, for 3 days. Cell number and differentiation into myofibroblasts were assessed by cell counting and immunocytostaining using a flow cytometer equipped with an autosampler (Thermo Fisher Scientific, Inc., Dreieich, Germany). α-Smooth muscle actin (αSMA) was used as a marker to distinguish myofibroblasts from fibroblasts. Fibroblasts were detached from the tissue culture plate using TrypLE (Gibco, Thermo Fisher Scientific, Inc., Dreieich, Germany), fixed with 4% paraformaldehyde (PFA, Sigma-Aldrich), permeabilized with 0.1% Triton X-100 (Sigma-Aldrich), and blocked for nonspecific binding with 1% bovine serum albumin (BSA, Sigma-Aldrich). Each step lasted 10 min, followed by a PBS wash. Cells were then stained with mouse antihuman αSMA antibody (1:500 dilution; clone: 1A4, Biolegend, San Diego, CA) for 1 h, followed by secondary staining with rabbit antimouse antibody conjugated to AlexaFluor 488 (Biolegend, San Diego, CA) for 30 min on ice. After washing, cells were analyzed by flow cytometry to quantify total cell number and αSMA-positive cells. As a positive control for fibroblast differentiation, cells were treated with 10 ng mL^{-1} TGF-β1 for 3 days.

4.18. Quantification of the Pro-inflammatory Response of Monocytes via NFKB Expression. THP-1 monocytic cells with the NFκB-GFP reporter gene were kindly provided by Dr. Xin Xie (Core Technology Platform, New York University Abu Dhabi, UAE). The cells were cultured in RPMI-1640 media supplemented with 10% FBS, 1% sodium pyruvate, 0.01% mercaptoethanol, and 1% penicillin/streptomycin at 37 °C, 5% CO_2, and 95% humidity. Cell culture media and supplements were purchased from Gibco (Thermo Fisher Scientific, Inc., Dreieich, Germany). To quantify the pro-inflammatory response, 5×10^5 cells were cultured with or without SAPs prepared at 2 mM (<CGC) for 24 h under standard cell culture conditions. As a positive control, the cells were treated with 10 ng mL^{-1} TNF-α (Biolegend, San Diego, CA), known to activate NFκB signaling. Cells were also treated with 10 ng mL^{-1} IFN-γ, as it is known to confirm the specificity of control because it does not trigger the NFkB signaling pathway. Subsequently, the cells were analyzed using an Attune NxT Flow Cytometer equipped with an autosampler (Thermo Fisher Scientific, Inc., Dreieich, Germany). Data analysis was performed using FlowJo software (Becton, Dickinson and Company, Franklin Lakes, NJ). The geometric mean fluorescence intensity (gMFI) of the NFκB-GFP reporter was evaluated. Experiments were performed in quadruplicate.

4.19. MΦ Differentiation from THP-1 Cells and Treatment with SAPs. For MΦ differentiation, 1×10^5 THP-1 cells (ATCC, Manassas, VA) were incubated with 300 nM phorbol-12-myristate-13-acetate (PMA; Sigma-Aldrich, Darmstadt, Germany) in RPMI-1640 media supplemented with 1% sodium pyruvate, 0.01% mercaptoethanol, and 1% penicillin/streptomycin but without fetal bovine serum (FBS), following previously published protocols.[10,59] The cell culture media and supplements were acquired from Gibco (Thermo Fisher Scientific, Inc., Dreieich, Germany). After 6 h, the differentiation medium was removed, and the cells were allowed to rest for 24 h in RPMI-1640 without FBS and PMA. Subsequently, the differentiated MΦs were cultured either with or without SAPs prepared at 2 mM for 48 h. As a control, MΦs were activated into pro-inflammatory (M1) MΦs for 48 h by adding 10 pg mL^{-1} lipopolysaccharide (LPS; Sigma) and 20 ng mL^{-1} interferon-γ (IFN-γ; Biolegend, San Diego, CA). For anti-inflammatory activation, MΦs were induced into the M2a subtype with 20 ng mL^{-1} interleukin 4 (IL-4; Biolegend) and 20 ng mL^{-1} interleukin 13 (IL-13; Biolegend), or into the M2c subtype with 20 ng mL^{-1} interleukin 10 (IL-10; Biolegend).

4.20. Quantitative Analysis of THP-1-Derived Macrophages (MΦs) Cytotoxicity, Cell Surface Markers, and Their Cytokine Secretion Profile. For analysis of MΦ cell surface markers, MΦs were detached from the cell culture plates using Macrophage Detachment Solution DXF (PromoCell, Heidelberg, Germany) following incubation with 2 mM SAPs or by placing on top of 20 mM SAP hydrogels. Before cell staining, they were incubated with Human TruStain FcX − Fc Receptor Blocking Solution (5 μL of blocking solution in 1000 μL of staining volume; Biolegend, San Diego, CA) for 5 min under standard cell culture conditions. Subsequently, the cells were stained with mouse antihuman HLA-DR (clone: L243) conjugated with Brilliant Violet 421, CD163 (Clone: GHI/61) conjugated with PE-Cy7, mouse antihuman CD206 (Clone: 15−2) conjugated with Brilliant Violet 510, and DRAQ7 (a cell viability staining dye) for 30 min on ice. The antibodies and DRAQ7 dye were diluted in PBS at a 1:250 ratio. All antibodies used in this study were sourced from Biolegend, San Diego, CA, USA. The stained cells were then analyzed using an Attune NxT Flow Cytometer equipped with an autosampler (Thermo Fisher Scientific, Inc., Dreieich, Germany), with compensation settings adjusted prior to analysis. Data analysis was conducted using FlowJo software (Becton, Dickinson and Company, Franklin Lakes, NJ), focusing on the geometric mean fluorescence intensity of the cell surface markers. Experiments were performed in 5 replicates for 2 mM SAPs and 4 replicates for 20 mM SAP hydrogels. For cytokine secretion profile analysis, cell culture supernatants were harvested following incubation with SAP products. The cytokine levels were quantified using a bead-based multiplex immunoassay (LEGENDplex Human Essential Immune Response Panel; Biolegend, San Diego, CA) designed for IL-4, IL-2, CXCL10 (IP-10), IL-1β, TNF-α, CCL2 (MCP-1), IL-17A, IL-6, IL-10, IFN-γ, IL-12p70, CXCL8 (IL-8), and TGF-β1, according to the manufacturer's protocol. The samples were analyzed on an Attune NxT Flow Cytometer (Thermo Fisher Scientific, Carlsbad, CA). Data were processed using a 5-parameter curve fitting algorithm with LEGENDplex data analysis software (Biolegend, San Diego, CA), and experiments were performed in 5 replicates.

4.21. Peripheral Blood Mononuclear Cells (PBMCs)-Derived Macrophages (MΦs) Cell Culture. Primary human monocytes were isolated from buffy coats purchased from the Regional Blood Donation Service SRK Graubünden (Chur, Switzerland) from five human donors (abbreviated as D1, D2, D3, D4, and D5) using Ficoll density gradient separation. Obtained peripheral blood mononuclear cells (PMBCs) were labeled with CD14 magnetic beads followed by magnetic-activated cell sorting.[82] CD14$^+$ monocyte cells were resuspended in RPMI medium supplemented with 10% FBS and then seeded onto tissue culture plastic at a density of 3×10^5 cells well^{-1} in the presence of 20 ng mL^{-1} human macrophage colony-stimulating factor (hM-CSF) for 5 days, similarly to our previous protocol.[38] Medium (still containing hM-CSF) was exchanged on day 2 (see Figure 8A for timing). At day 5, the hM-CSF-free medium was supplemented with 10 ng mL^{-1} TNF-α and 10 ng mL^{-1} IFN-γ for M1 MΦs and 10 ng mL^{-1} IL-4 for M2 MΦs for 24 h followed by a 24 h rest in medium without cytokines (see Figure 8A for timing). Control samples (M0 MΦs) were cultured in a medium without any cytokines. Furthermore, on day 5, the same three polarization states were maintained (M0, M1, M2), either without any external influence of materials or in the presence of the 2 mM SAPs supplemented in the cell culture medium. Noteworthy, 2 mM of all SAPs was below CGC to maintain the supplementation of nanostructure form (<CGC, solution form) and did not result in the formation of any self-supporting physical hydrogels. On day 7, a conditioned medium was collected for ELISA, whereas samples were washed two times with PBS and stored in TRI-reagent for subsequent RNA isolation.

4.22. Enzyme-Linked Immunosorbent Assay (ELISA). At the end of each polarization experiment, supernatant media was collected and kept for measurements of pro-inflammatory (IL-6, TNF-α) and anti-inflammatory (CD163, IL-10, IL-12) cytokines, associated with M1 and M2 MΦs, respectively. The DuoSet ELISA systems were used according to the manufacturer's instructions of DY210 (TNF-α) R&D Systems. Absorbance values were measured on an Infinite 200

https://doi.org/10.1021/acsami.4c19900
ACS Appl. Mater. Interfaces 2025, 17, 27740−27758

Pro plate reader (Tecan, Männedorf, Switzerland) at 450 nm with a background wavelength correction of 540 nm.

4.23. RNA Isolation and RT-qPCR Gene Analysis. To assess the polarization of MΦs, cells were collected and seeded in a 24-well plate at a concentration and with treatments described above. RNA was isolated with salt precipitation and TaqManTM Reverse Transcription Kit was used to generate cDNA. Relative gene expression reactions were set up in 10 μL reaction mixes using TaqManTM MasterMix, relevant human primers (Table 1), diethyl pyrocarbonate treated water (DEPC-water), and cDNA. Real-time polymerase chain reaction (real-time PCR) was performed on two technical replicates for $n = 3$ repeats, using QuantStudio 7 Flex. The relative gene expression was identified using a $2^{-\Delta\Delta Ct}$ value with RPLP0 as endogenous control and positive control (M0 MΦs, no supplemented material or cytokines) was used for normalization. Normalization was performed per each donor, i.e., all relative expression are normalized to the M0 untreated control group of each donor.

Table 1. Human Primer Sequences for Real-Time PCR

marker	assay ID (THERMOFISHER)	role
TNF-α	Hs00174128_m1	pro-inflammatory marker (associated with M1 MΦs)
MRC1 (CD206)	Hs00267207_m1	surface marker for M2 MΦs
RPLP0	Forward: *5′-TGG GCA AGA ACA CCA TGA TG-3′*	housekeeping gene
	Reverse: *5′-CGG ATA TGA GGC AGC AGT TTC-3*	
	Probe: *5′-AGG GCA CCT GGA AAA CAA CCC AGC-3′*	

4.24. Statistical Analysis. All results were analyzed and presented with GraphPad Prism version 9.3.1. Results are shown as an average ± standard deviation (SD), with individual points marked. To perform statistical significance one-way analysis of variance (ANOVA) with Šídák's multiple comparisons, Tukey's multiple comparisons test, or Kruskal–Wallis multiple comparisons was used and noted in each case in Figure description. Statistically significant results were considered as of $p < 0.05$ (ns - >0.05, * - <0.05, ** - <0.01, *** - <0.005, and **** - <0.001).

■ ASSOCIATED CONTENT

Supporting Information

The Supporting Information is available free of charge at https://pubs.acs.org/doi/10.1021/acsami.4c19900.

Photographs of gelation of all SAP hydrogels; ThT assays; CD spectroscopy; molecular dynamics conformation and H-bonding calculations; Amplitude and frequency sweeps of all SAP hydrogels; Oscillatory rheology recovery of tyrosine-containing SAP hydrogels and supporting digital photographs of printed rings in other conditions. Cytotoxicity studies of SAPs on fibroblasts. Additional immunological data (flow cytometry, PCR) for macrophage polarization studies (PDF)

SM1 Molecular dynamics simulation for **EF8** (MOV)

SM2 Molecular dynamics simulation for **YEF8** (MOV)

SM3 Molecular dynamics simulation for **EF8Y** (MOV)

SM4 Molecular dynamics simulation for **YEF8Y** (MOV)

SM5 Molecular dynamics simulation for **EYF8** (MOV)

■ AUTHOR INFORMATION

Corresponding Author

Jacek K. Wychowaniec − *AO Research Institute Davos, Davos 7270, Switzerland;* orcid.org/0000-0002-6597-5242; Email: jacek.wychowaniec@aofoundation.org

Authors

Ezgi Irem Bektas − *AO Research Institute Davos, Davos 7270, Switzerland*

Marcia Muerner − *AO Research Institute Davos, Davos 7270, Switzerland; ETH Zürich, Zürich 8092, Switzerland*

Jiranuwat Sapudom − *Laboratory for Immuno Bioengineering Research and Applications, Division of Engineering, New York University Abu Dhabi, Abu Dhabi 129188, United Arab Emirates;* orcid.org/0000-0001-6627-7713

Martin Šrejber − *Regional Centre of Advanced Technologies and Materials, Czech Advanced Technology and Research Institute (CATRIN), Palacký University Olomouc, 779 00 Olomouc, Czech Republic;* orcid.org/0000-0001-9556-2978

Marielle Airoldi − *AO Research Institute Davos, Davos 7270, Switzerland*

Roland Schmidt − *Hitachi High-Tech Europe GmbH, 47807 Krefeld, Germany*

Andrea J. Vernengo − *AO Research Institute Davos, Davos 7270, Switzerland;* Present Address: Departments of Chemical Engineering and Biomedical Engineering, Henry M. Rowan College of Engineering, Rowan University, Glassboro, New Jersey 08028, USA; orcid.org/0000-0002-5143-7435

Charlotte J. C. Edwards-Gayle − *Diamond Light Source, Harwell Science and Innovation Campus, Didcot OX110DE, United Kingdom*

Paul Sean Tipay − *Laboratory for Immuno Bioengineering Research and Applications, Division of Engineering, New York University Abu Dhabi, Abu Dhabi 129188, United Arab Emirates*

Michal Otyepka − *Regional Centre of Advanced Technologies and Materials, Czech Advanced Technology and Research Institute (CATRIN), Palacký University Olomouc, 779 00 Olomouc, Czech Republic; IT4Innovations, VSB-Technical University of Ostrava, 708 00 Ostrava-Poruba, Czech Republic;* orcid.org/0000-0002-1066-5677

Jeremy Teo − *Laboratory for Immuno Bioengineering Research and Applications, Division of Engineering, New York University Abu Dhabi, Abu Dhabi 129188, United Arab Emirates;* orcid.org/0000-0001-6869-3833

David Eglin − *Mines Saint-Étienne, Univ Jean Monnet, INSERM, UMR, 1059 Saint-Étienne, France*

Matteo D'Este − *AO Research Institute Davos, Davos 7270, Switzerland;* orcid.org/0000-0002-0424-8172

Complete contact information is available at: https://pubs.acs.org/10.1021/acsami.4c19900

Author Contributions

J.K.W.: Conceptualization, data curation, formal analysis, funding acquisition, investigation, methodology, project administration, resources, supervision, validation, visualization, writing—original draft, writing—review and editing; E.I.B.: Data curation, investigation, formal analysis, methodology, writing—review and editing; J.S. Data curation, investigation, methodology, formal analysis, writing—review and editing; M.M.: Data curation, investigation, methodology, writing—

https://doi.org/10.1021/acsami.4c19900
ACS Appl. Mater. Interfaces 2025, 17, 27740−27758

review and editing; M.Š.: Data curation, investigation, methodology, writing—review and editing; M.A.: Data curation, investigation, methodology, writing—review and editing; R.S.: Data curation, methodology, writing—review and editing; A.J.V.: Data curation, investigation, methodology, writing—review and editing; C.J.C.E-G.: Data curation, methodology; P.S.T.: Data curation, methodology; M.O. Resources, methodology, supervision; J.T. Conceptualization, resources, funding acquisition, supervision, writing—review and editing; D.E.: Conceptualization, resources, funding acquisition, supervision, writing—review and editing; M.D.: Conceptualization, funding acquisition, resources, methodology, project administration, resources, supervision, writing—review and editing.

Funding

This work was supported by the European Union's Horizon 2020 (H2020-MSCA-IF-2019) research and innovation program under the Marie Skłodowska-Curie grant agreement 893099—ImmunoBioInks; by the Leading House for the Middle East and North Africa for Research Partnership Grant 2022 "Space ImmunoBioInks" (RPG-2022−38) and Consolidation 2023 "SI-WHIM" (COG-2023−35) grants. This publication is based upon work from COST Action SNOOPY (CA23111) supported by COST (European Cooperation in Science and Technology). J.K.W. is also grateful to DLS (Didcot, UK) for awarding beam time (SM29767) to this project. J.K.W. and M.D'E. also acknowledge the European Union's Horizon 2020 research and innovation program under grant agreement No 857287 (BBCE), as well as funding provided by AO Foundation. M.Š. and M.O. acknowledge the support by the ERDF/ESF project TECHSCALE (No. CZ.02.01.01/00/22_008/0004587) and the Ministry of Education, Youth and Sports of the Czech Republic through the e-INFRA CZ (ID: 90254).

Notes

The authors declare no competing financial interest.

All research data supporting this publication are directly available within this publication and associated Supporting Information.

■ ACKNOWLEDGMENTS

The authors thank Nicolas Devantay for his technical support and Dr. Ursula Menzel for her assistance with PCR plating. J.K.W. and D.E. thank Nora Mallouk-Forges of the Centre de Microscopie Electronique Stéphanois for technical support. The authors would also like to acknowledge the support from Molecular and Cell Biology core technology platform at New York University Abu Dhabi. The authors acknowledge the support from Yves Jaccaud from Portmann Instruments AG for facilitating contact for SEM measurements. The authors thank Clara Presciutti for her support with L929 fibroblast culture maintenance. This work benefited from the use of the SasView application, originally developed under NSF award DMR-0520547. SasView contains code developed with funding from the European Union's Horizon 2020 research and innovation program under the SINE2020 project, grant agreement No 654000.

■ REFERENCES

(1) Mao, J.; Chen, L.; Cai, Z.; Qian, S.; Liu, Z.; Zhao, B.; Zhang, Y.; Sun, X.; Cui, W. Advanced Biomaterials for Regulating Polarization of Macrophages in Wound Healing. *Adv. Funct. Mater.* **2022**, *32* (12), No. 2111003.

(2) Bucher, C. H.; Schlundt, C.; Wulsten, D.; Sass, F. A.; Wendler, S.; Ellinghaus, A.; Thiele, T.; Seemann, R.; Willie, B. M.; Volk, H.-D.; et al. Experience in the Adaptive Immunity Impacts Bone Homeostasis, Remodeling, and Healing. *Front. Immunol.* **2019**, *10*, No. 797.

(3) Zhang, B.; Su, Y.; Zhou, J.; Zheng, Y.; Zhu, D. Toward a Better Regeneration through Implant-Mediated Immunomodulation: Harnessing the Immune Responses. *Adv. Sci.* **2021**, *8* (16), No. 2100446.

(4) Kigerl, K. A.; Gensel, J. C.; Ankeny, D. P.; Alexander, J. K.; Donnelly, D. J.; Popovich, P. G. Identification of Two Distinct Macrophage Subsets with Divergent Effects Causing either Neurotoxicity or Regeneration in the Injured Mouse Spinal Cord. *J. Neurosci.* **2009**, *29* (43), 13435−13444.

(5) Fang, P.; Li, X.; Dai, J.; Cole, L.; Camacho, J. A.; Zhang, Y.; Ji, Y.; Wang, J.; Yang, X. F.; Wang, H. Immune cell subset differentiation and tissue inflammation. *J. Hematol. Oncol.* **2018**, *11* (1), No. 97.

(6) Krzyszczyk, P.; Schloss, R.; Palmer, A.; Berthiaume, F. The Role of Macrophages in Acute and Chronic Wound Healing and Interventions to Promote Pro-wound Healing Phenotypes. *Front. Physiol.* **2018**, *9*, No. 419, DOI: 10.3389/fphys.2018.00419.

(7) Duque, G. A.; Descoteaux, A. Macrophage Cytokines: Involvement in Immunity and Infectious Diseases. *Front. Immunol.* **2014**, *5*, No. 491, DOI: 10.3389/fimmu.2014.00491.

(8) Gordon, S. Alternative activation of macrophages. *Nat. Rev. Immunol.* **2003**, *3* (1), 23−35, DOI: 10.1038/nri978.

(9) Lawrence, T.; Natoli, G. Transcriptional regulation of macrophage polarization: enabling diversity with identity. *Nat. Rev. Immunol.* **2011**, *11* (11), 750−761.

(10) Sapudom, J.; Karaman, S.; Mohamed, W. K. E.; Garcia-Sabate, A.; Quartey, B. C.; Teo, J. C. M. 3D in vitro M2 macrophage model to mimic modulation of tissue repair. *npj Regener. Med.* **2021**, *6* (1), No. 83.

(11) Walsh, C. M.; Wychowaniec, J. K.; Brougham, D. F.; Dooley, D. Functional hydrogels as therapeutic tools for spinal cord injury: New perspectives on immunopharmacological interventions. *Pharmacol. Ther.* **2022**, *234*, No. 108043.

(12) García-García, A.; Pigeot, S.; Martin, I. Engineering of immunoinstructive extracellular matrices for enhanced osteoinductivity. *Bioact. Mater.* **2023**, *24*, 174−184.

(13) Halperin-Sternfeld, M.; Pokhojaev, A.; Ghosh, M.; Rachmiel, D.; Kannan, R.; Grinberg, I.; Asher, M.; Aviv, M.; Ma, P. X.; Binderman, I.; et al. Immunomodulatory fibrous hyaluronic acid-Fmoc-diphenylalanine-based hydrogel induces bone regeneration. *J. Clin. Periodontol.* **2023**, *50* (2), 200−219, DOI: 10.1111/jcpe.13725.

(14) Nakkala, J. R.; Yao, Y.; Zhai, Z.; Duan, Y.; Zhang, D.; Mao, Z.; Lu, L.; Gao, C. Dimethyl Itaconate-Loaded Nanofibers Rewrite Macrophage Polarization, Reduce Inflammation, and Enhance Repair of Myocardic Infarction. *Small* **2021**, *17* (17), No. e2006992.

(15) Taskin, M. B.; Tylek, T.; Blum, C.; Bohm, C.; Wiesbeck, C.; Groll, J. Inducing Immunomodulatory Effects on Human Macrophages by Multifunctional NCO-sP(EO-stat-PO)/Gelatin Hydrogel Nanofibers. *ACS Biomater Sci. Eng.* **2021**, *7* (7), 3166−3178.

(16) Kumar, V. A.; Taylor, N. L.; Shi, S.; Wickremasinghe, N. C.; D'Souza, R. N.; Hartgerink, J. D. Self-assembling multidomain peptides tailor biological responses through biphasic release. *Biomaterials* **2015**, *52*, 71−78.

(17) Whitesides, G. M.; Grzybowski, B. Self-assembly at all scales. *Science* **2002**, *295* (5564), 2418−2421.

(18) Edwards-Gayle, C. J. C.; Wychowaniec, J. K. Characterization of Peptide-Based Nanomaterials. In *Peptide Bionanomaterials*; Elsawy, M. A., Ed.; Springer International Publishing, 2023; pp 255−308.

(19) Ligorio, C.; Mata, A. Synthetic extracellular matrices with function-encoding peptides. *Nat. Rev. Bioeng* **2023**, *1* (7), 518−536.

(20) Pappas, C. G.; Shafi, R.; Sasselli, I. R.; Siccardi, H.; Wang, T.; Narang, V.; Abzalimov, R.; Wijerathne, N.; Ulijn, R. V. Dynamic peptide libraries for the discovery of supramolecular nanomaterials. *Nat. Nanotechnol.* **2016**, *11* (11), 960−967.

(21) Sheehan, F.; Sementa, D.; Jain, A.; Kumar, M.; Tayarani-Najjaran, M.; Kroiss, D.; Ulijn, R. V. Peptide-Based Supramolecular Systems Chemistry. *Chem. Rev.* **2021**, *121*, 13869−13914.
(22) Garcia, A. M.; Melchionna, M.; Bellotto, O.; Kralj, S.; Semeraro, S.; Parisi, E.; Iglesias, D.; D'Andrea, P.; De Zorzi, R.; Vargiu, A. V.; Marchesan, S. Nanoscale Assembly of Functional Peptides with Divergent Programming Elements. *ACS Nano* **2021**, *15* (2), 3015−3025.
(23) Soliman, M. A. N.; Khedr, A.; Sahota, T.; Armitage, R.; Allan, R.; Laird, K.; Allcock, N.; Ghuloum, F. I.; Amer, M. H.; Alazragi, R.; et al. Unraveling the Atomistic Mechanism of Electrostatic Lateral Association of Peptide β-Sheet Structures and Its Role in Nanofiber Growth and Hydrogelation. *Small* **2025**, *21*, No. 2408213.
(24) Wychowaniec, J. K.; Patel, R.; Leach, J.; Mathomes, R.; Chhabria, V.; Patil-Sen, Y.; Hidalgo-Bastida, A.; Forbes, R. T.; Hayes, J. M.; Elsawy, M. A. Aromatic Stacking Facilitated Self-Assembly of Ultrashort Ionic Complementary Peptide Sequence: beta-Sheet Nanofibers with Remarkable Gelation and Interfacial Properties. *Biomacromolecules* **2020**, *21* (7), 2670−2680.
(25) Geckil, H.; Xu, F.; Zhang, X. H.; Moon, S.; Demirci, U. Engineering hydrogels as extracellular matrix mimics. *Nanomedicine* **2010**, *5* (3), 469−484.
(26) Nguyen, A. K.; Molley, T. G.; Kardia, E.; Ganda, S.; Chakraborty, S.; Wong, S. L.; Ruan, J.; Yee, B. E.; Mata, J.; Vijayan, A.; et al. Hierarchical assembly of tryptophan zipper peptides into stress-relaxing bioactive hydrogels. *Nat. Commun.* **2023**, *14* (1), No. 6604.
(27) Treacy, N. J.; Clerkin, S.; Davis, J. L.; Kennedy, C.; Miller, A. F.; Saiani, A.; Wychowaniec, J. K.; Brougham, D. F.; Crean, J. Growth and differentiation of human induced pluripotent stem cell (hiPSC)-derived kidney organoids using fully synthetic peptide hydrogels. *Bioact. Mater.* **2023**, *21*, 142−156.
(28) Zhang, S.; Altman, M. Peptide self-assembly in functional polymer science and engineering. *React. Funct. Polym.* **1999**, *41* (1), 91−102.
(29) Elsawy, M. A.; Wychowaniec, J. K.; Castillo Diaz, L. A.; Smith, A. M.; Miller, A. F.; Saiani, A. Controlling Doxorubicin Release from a Peptide Hydrogel through Fine-Tuning of Drug-Peptide Fiber Interactions. *Biomacromolecules* **2022**, *23* (6), 2624−2634.
(30) Wychowaniec, J. K.; Smith, A. M.; Ligorio, C.; Mykhaylyk, O. O.; Miller, A. F.; Saiani, A. Role of Sheet-Edge Interactions in β-sheet Self-Assembling Peptide Hydrogels. *Biomacromolecules* **2020**, *21*, 2285−2297.
(31) Si, Y.; Wen, Y.; Kelly, S. H.; Chong, A. S.; Collier, J. H. Intranasal delivery of adjuvant-free peptide nanofibers elicits resident CD8+ T cell responses. *J. Controlled Release* **2018**, *282*, 120−130.
(32) Votaw, N. L.; Collier, L.; Curvino, E. J.; Wu, Y.; Fries, C. N.; Ojeda, M. T.; Collier, J. H. Randomized peptide assemblies for enhancing immune responses to nanomaterials. *Biomaterials* **2021**, *273*, No. 120825.
(33) Mora-Solano, C.; Wen, Y.; Han, H.; Chen, J.; Chong, A. S.; Miller, M. L.; Pompano, R. R.; Collier, J. H. Active immunotherapy for TNF-mediated inflammation using self-assembled peptide nanofibers. *Biomaterials* **2017**, *149*, 1−11.
(34) Rudra, J. S.; Sun, T.; Bird, K. C.; Daniels, M. D.; Gasiorowski, J. Z.; Chong, A. S.; Collier, J. H. Modulating Adaptive Immune Responses to Peptide Self-Assemblies. *ACS Nano* **2012**, *6* (2), 1557−1564.
(35) Wen, Y.; Waltman, A.; Han, H.; Collier, J. H. Switching the Immunogenicity of Peptide Assemblies Using Surface Properties. *ACS Nano* **2016**, *10* (10), 9274−9286.
(36) Lee, J.; Ju, M.; Cho, O. H.; Kim, Y.; Nam, K. T. Tyrosine-Rich Peptides as a Platform for Assembly and Material Synthesis. *Adv. Sci.* **2019**, *6* (4), No. 1801255.
(37) Ding, Y.; Li, Y.; Qin, M.; Cao, Y.; Wang, W. Photo-Cross-Linking Approach to Engineering Small Tyrosine-Containing Peptide Hydrogels with Enhanced Mechanical Stability. *Langmuir* **2013**, *29* (43), 13299−13306.
(38) Wychowaniec, J. K.; Bektas, E. I.; Vernengo, A. J.; Muerner, M.; Airoldi, M.; Tipay, P. S.; Sapudom, J.; Teo, J.; Eglin, D.; D'Este, M. Effect of molecular weight of tyramine-modified hyaluronan on polarization state of THP-1 and peripheral blood mononuclear cells-derived macrophages. *Biomater. Adv.* **2025**, *169*, No. 214166.
(39) Marinho, A.; Nunes, C.; Reis, S. Hyaluronic Acid: A Key Ingredient in the Therapy of Inflammation. *Biomolecules* **2021**, *11*, No. 1518, DOI: 10.3390/biom11101518.
(40) Schwarz, D.; Lipoldová, M.; Reinecke, H.; Sohrabi, Y. Targeting inflammation with collagen. *Clin. Transl. Med.* **2022**, *12* (5), No. e831.
(41) Wychowaniec, J. K.; Moffat, J.; Saiani, A. Quantitative nanomechanical properties evaluation of a family of beta-sheet peptide fibres using rapid bimodal AFM. *J. Mech. Behav. Biomed. Mater.* **2021**, *124*, No. 104776.
(42) Nelson, D. L.; Lehninger, A. L.; Cox, M. M. Lehninger Principles of biochemistry. 2017.
(43) Pace, C. N.; Horn, G.; Hebert, E. J.; Bechert, J.; Shaw, K.; Urbanikova, L.; Scholtz, J. M.; Sevcik, J. Tyrosine hydrogen bonds make a large contribution to protein stability. *J. Mol. Biol.* **2001**, *312* (2), 393−404.
(44) Caplan, M. R.; Moore, P. N.; Zhang, S. G.; Kamm, R. D.; Lauffenburger, D. A. Self-assembly of a beta-sheet protein governed by relief of electrostatic repulsion relative to van der Waals attraction. *Biomacromolecules* **2000**, *1* (4), 627−631.
(45) Xing, Z.; Chen, Y.; Qiu, F. Alternative Causal Link between Peptide Fibrillization and β-Strand Conformation. *ACS Omega* **2021**, *6* (19), 12904−12912.
(46) Aggeli, A.; Bell, M.; Carrick, L. M.; Fishwick, C. W. G.; Harding, R.; Mawer, P. J.; Radford, S. E.; Strong, A. E.; Boden, N. pH as a Trigger of Peptide β-Sheet Self-Assembly and Reversible Switching between Nematic and Isotropic Phases. *J. Am. Chem. Soc.* **2003**, *125* (32), 9619−9628.
(47) Barth, A. Infrared spectroscopy of proteins. *Biochim. Biophys. Acta, Bioenerg.* **2007**, *1767* (9), 1073−1101.
(48) Rodger, A.; Chubb, J. J. Circular Dichroism and Linear Dichroism. In *Encyclopedia of Analytical Chemistry*; Wiley, 2007; pp 1−42.
(49) Sreerama, N.; Woody, R. W. A Self-Consistent Method for the Analysis of Protein Secondary Structure from Circular Dichroism. *Anal. Biochem.* **1993**, *209* (1), 32−44.
(50) Sreerama, N.; Woody, R. W. Estimation of Protein Secondary Structure from Circular Dichroism Spectra: Comparison of CONTIN, SELCON, and CDSSTR Methods with an Expanded Reference Set. *Anal. Biochem.* **2000**, *287* (2), 252−260.
(51) Chaudhuri, O.; Cooper-White, J.; Janmey, P. A.; Mooney, D. J.; Shenoy, V. B. Effects of extracellular matrix viscoelasticity on cellular behaviour. *Nature* **2020**, *584* (7822), 535−546.
(52) Guimarães, C. F.; Gasperini, L.; Marques, A. P.; Reis, R. L. The stiffness of living tissues and its implications for tissue engineering. *Nat. Rev. Mater.* **2020**, *5* (5), 351−370.
(53) Dong, S.; Chapman, S. L.; Pluen, A.; Richardson, S. M.; Miller, A. F.; Saiani, A. Effect of Peptide−Polymer Host−Guest Electrostatic Interactions on Self-Assembling Peptide Hydrogels Structural and Mechanical Properties and Polymer Diffusivity. *Biomacromolecules* **2024**, *25* (6), 3628−3641.
(54) Schwab, A.; Levato, R.; D'Este, M.; Piluso, S.; Eglin, D.; Malda, J. Printability and Shape Fidelity of Bioinks in 3D Bioprinting. *Chem. Rev.* **2020**, *120* (19), 11028−11055.
(55) Singh, K.; Wychowaniec, J. K.; Edwards-Gayle, C. J. C.; Reynaud, E. G.; Rodriguez, B. J.; Brougham, D. F. Structure-dynamics correlations in composite PF127-PEG-based hydrogels; cohesive/hydrophobic interactions determine phase and rheology and identify the role of micelle concentration in controlling 3D extrusion printability. *J. Colloid Interface Sci.* **2024**, *660*, 302−313.
(56) Chiesa, I.; Ligorio, C.; Bonatti, A. F.; De Acutis, A.; Smith, A. M.; Saiani, A.; Vozzi, G.; De Maria, C. Modeling the Three-Dimensional Bioprinting Process of beta-Sheet Self-Assembling Peptide Hydrogel Scaffolds. *Front. Med. Technol.* **2020**, *2*, No. 571626.

(57) Liu, T.; Zhang, L.; Joo, D.; Sun, S.-C. NF-κB signaling in inflammation. *Signal Transduction Targeted Ther.* **2017**, *2* (1), No. 17023.
(58) Zhi, Y.; Lu, H.; Duan, Y.; Sun, W.; Guan, G.; Dong, Q.; Yang, C. Involvement of the nuclear factor-κB signaling pathway in the regulation of CXC chemokine receptor-4 expression in neuroblastoma cells induced by tumor necrosis factor-α. *Int. J. Mol. Med.* **2015**, *35* (2), 349−357.
(59) Sapudom, J.; Mohamed, W. K. E.; Garcia-Sabate, A.; Alatoom, A.; Karaman, S.; Mahtani, N.; Teo, J. C. Collagen Fibril Density Modulates Macrophage Activation and Cellular Functions during Tissue Repair. *Bioengineering* **2020**, *7* (2), No. 33.
(60) Sapudom, J.; Karaman, S.; Mohamed, W. K. E.; Garcia-Sabaté, A.; Quartey, B. C.; Teo, J. C. M. 3D in vitro M2 macrophage model to mimic modulation of tissue repair. *npj Regener. Med.* **2021**, *6* (1), No. 83.
(61) Sapudom, J.; Wu, X.; Chkolnikov, M.; Ansorge, M.; Anderegg, U.; Pompe, T. Fibroblast fate regulation by time dependent TGF-β1 and IL-10 stimulation in biomimetic 3D matrices. *Biomater. Sci.* **2017**, *5* (9), 1858−1867.
(62) Schruefer, R.; Lutze, N.; Schymeinsky, J.; Walzog, B. Human neutrophils promote angiogenesis by a paracrine feedforward mechanism involving endothelial interleukin-8. *Am. J. Physiol.: Heart Circ. Physiol.* **2005**, *288* (3), H1186−H1192.
(63) Nelson, B. H. IL-2, Regulatory T Cells, and Tolerance. *J. Immunol.* **2004**, *172* (7), 3983−3988.
(64) Wang, D.; Bratlie, K. M. Influence of Polymer Chemistry on Cytokine Secretion from Polarized Macrophages. *ACS Biomater. Sci. Eng.* **2015**, *1* (3), 166−174.
(65) Hedrich, C. M.; Bream, J. Cell type-specific regulation of IL-10 expression in inflammation and disease. *Immunol. Res.* **2010**, *47*, 185−206.
(66) Kozicky, L. K.; Menzies, S. C.; Zhao, Z. Y.; Vira, T.; Harnden, K.; Safari, K.; Del Bel, K. L.; Turvey, S. E.; Sly, L. M. IVIg and LPS Co-stimulation Induces IL-10 Production by Human Monocytes, Which Is Compromised by an FcgammaRIIA Disease-Associated Gene Variant. *Front. Immunol.* **2018**, *9*, No. 2676.
(67) Haddy, N.; Sass, C.; Maumus, S.; Marie, B.; Droesch, S.; Siest, G.; Lambert, D.; Visvikis, S. Biological variations, genetic polymorphisms and familial resemblance of TNF-α and IL-6 concentrations: STANISLAS cohort. *Eur. J. Hum. Genet.* **2005**, *13* (1), 109−117.
(68) Hou, J.; Yang, R.; Vuong, I.; Li, F.; Kong, J.; Mao, H. Q. Biomaterials strategies to balance inflammation and tenogenesis for tendon repair. *Acta Biomater.* **2021**, *130*, 1−16.
(69) Faroni, A.; Workman, V. L.; Saiani, A.; Reid, A. J. Self-Assembling Peptide Hydrogel Matrices Improve the Neurotrophic Potential of Human Adipose-Derived Stem Cells. *Adv. Healthcare Mater.* **2019**, *8* (17), No. e1900410.
(70) Miles, A. J.; Ramalli, S. G.; Wallace, B. A. DichroWeb, a website for calculating protein secondary structure from circular dichroism spectroscopic data. *Protein Sci.* **2022**, *31* (1), 37−46.
(71) Schrodinger, L. L. C.*The PyMOL molecular graphics system*, 2010.
(72) Case, D. A.; Aktulga, H. M.; Belfon, K.; Ben-Shalom, I.; Brozell, S. R.; Cerutti, D. S.; Cheatham, T. E., III; Cruzeiro, V. W. D.; Darden, T. A.; Duke, R. E. *Amber 2021*; University of California: San Francisco, 2021.
(73) Tian, C.; Kasavajhala, K.; Belfon, K. A. A.; Raguette, L.; Huang, H.; Migues, A. N.; Bickel, J.; Wang, Y.; Pincay, J.; Wu, Q.; Simmerling, C. ff19SB: Amino-Acid-Specific Protein Backbone Parameters Trained against Quantum Mechanics Energy Surfaces in Solution. *J. Chem. Theory Comput.* **2020**, *16* (1), 528−552.
(74) Izadi, S.; Anandakrishnan, R.; Onufriev, A. V. Building Water Models: A Different Approach. *J. Phys. Chem. Lett.* **2014**, *5* (21), 3863−3871.
(75) Sengupta, A.; Li, Z.; Song, L. F.; Li, P.; Merz, K. M., Jr. Parameterization of Monovalent Ions for the OPC3, OPC, TIP3P-FB, and TIP4P-FB Water Models. *J. Chem. Inf. Model.* **2021**, *61* (2), 869−880.
(76) Berendsen, H. J. C.; Postma, J. P. M.; van Gunsteren, W. F.; DiNola, A.; Haak, J. R. Molecular dynamics with coupling to an external bath. *J. Chem. Phys.* **1984**, *81* (8), 3684−3690.
(77) Ryckaert, J.-P.; Ciccotti, G.; Berendsen, H. J. C. Numerical integration of the cartesian equations of motion of a system with constraints: molecular dynamics of n-alkanes. *J. Comput. Phys.* **1977**, *23* (3), 327−341.
(78) Darden, T.; York, D.; Pedersen, L. Particle mesh Ewald: An N·log(N) method for Ewald sums in large systems. *J. Chem. Phys.* **1993**, *98* (12), 10089−10092.
(79) Cowieson, N. P.; Edwards-Gayle, C. J. C.; Inoue, K.; Khunti, N. S.; Doutch, J.; Williams, E.; Daniels, S.; Preece, G.; Krumpa, N. A.; Sutter, J. P.; et al. Beamline B21: high-throughput small-angle X-ray scattering at Diamond Light Source. *J. Synchrotron Radiat.* **2020**, *27* (Pt 5), 1438−1446.
(80) Edwards-Gayle, C. J. C.; Khunti, N.; Hamley, I. W.; Inoue, K.; Cowieson, N.; Rambo, R. Design of a multipurpose sample cell holder for the Diamond Light Source high-throughput SAXS beamline B21. *J. Synchrotron Radiat.* **2021**, *28* (1), 318−321.
(81) Hinton, T. J.; Hudson, A.; Pusch, K.; Lee, A.; Feinberg, A. W. 3D Printing PDMS Elastomer in a Hydrophilic Support Bath via Freeform Reversible Embedding. *ACS Biomater. Sci. Eng.* **2016**, *2* (10), 1781−1786.
(82) Razzi, F.; Fratila-Apachitei, L. E.; Fahy, N.; Bastiaansen-Jenniskens, Y. M.; Apachitei, I.; Farrell, E.; Zadpoor, A. A. Immunomodulation of surface biofunctionalized 3D printed porous titanium implants. *Biomed. Mater.* **2020**, *15* (3), No. 035017.

https://doi.org/10.1021/acsami.4c19900
ACS Appl. Mater. Interfaces 2025, 17, 27740−27758